A-Brick ASTF

Exploring feasibility of engineering an Active Solar Thermal Façade based on A-Brick system

Linfeng Zhou

08.01.2025

TU Delft

Mentors:
Dr.ing. M. Bilow
Ir. E.R. van den Ham

Master's Thesis Research Report P5

TU Delft Faculty of Architecture & the Built Environment

MSc of Building Technology at Department of
Architectural Engineering and Technologies (AE+T)

Author: **Linfeng Zhou**

First Mentor: **Dr.ing. M. Bilow**

Second Mentor: **Ir. E.R. van den Ham**

A-Brick ASTF

Exploring feasibility of engineering an Active Solar Thermal Façade (ASTF) product based on A-Brick system

Abstract

This study investigates the feasibility of transforming Aberson's A-Brick ventilated ceramic façade into an effective Active Solar Thermal Façade (ASTF) system and evaluates its thermal performance across multiple energy applications. A combination of literature review, laboratory prototype experiments, ANSYS CFD simulations, numerical calculations, and TRNSYS annual modelling is employed to assess both heat-collector and heat-exchanger operation modes. Prototype results show that the unglazed ceramic façade achieves moderate solar-collector performance, with efficiency of 15–30%, heat-removal factors of 0.25–0.35, and a relatively high heat-loss coefficient due to direct exposure and limited thermal coupling. When operating as a heat exchanger, the system delivers an overall heat-transfer coefficient of 14–25 W/m²K, strongly governed by air-side convection. Despite lower thermal performance compared with glazed collectors or fan-coil evaporators, the façade's large usable surface compensates for these limitations.

System-level analyses demonstrate that a 10.77 m² south-facing façade can preheat 200 L of domestic hot water during spring–summer conditions, while approximately 22.8 m² of façade area is sufficient to meet the evaporator load of a 6 kW heat pump under Dutch winter design conditions. TRNSYS simulations further indicate that the integrated façade–heat-pump system can achieve a seasonal COP of around 4.2. The results confirm that the A-Brick system can be engineered into a functional ASTF with promising potential for DHW preheating and heat-pump applications, providing a viable façade-integrated renewable energy solution for residential buildings.

Content

Abbreviations

ASTF: Active Solar Thermal Facades
COP: Coefficient of performance
DHW: Domestic hot water system
SAHP: Solar assisted heat pump
DX-SAHP: Direct Solar assisted heat pump
IDX-SAHP: Indirect Solar assisted heat pump
ASHP: Air source heat pump

Nomenclature

$\mathbf{G}$	Solar irradiance (W/m^2)
$\boldsymbol{\tau\alpha}$	Transmittance and absorptance
$\mathbf{F_R}$	Heat removal factor
$\boldsymbol{\eta}$	Average solar collector efficiency
$\boldsymbol{\eta_c}$	Carnot efficiency of heat pump
$\mathbf{h_L}$	Overall heat-loss coefficient (W/m^2K)
$\mathbf{h_{sys}}$	Overall heat-transfer coefficient (W/m^2K)
$\mathbf{A}$	Effective heat-exchanging surface area (m^2)
$\mathbf{T_{pl}}$	Absorber Plate (ceramic claddings) temperature (K)
$\mathbf{T_a}$	Ambient air temperature (K)
$\mathbf{T_{out}}$	Fluid outlet temperature (K)
$\mathbf{T_{in}}$	Fluid inlet temperature (K)
$\mathbf{T_0}$	Initial tap water temperature(K)
$\mathbf{T_h}$	Hot side (load)temperature (K)
$\mathbf{T_c}$	Cold side (source) temperature (K)
$\mathbf{T_{cond}}$	Condensing temperature (K)
$\mathbf{T_{evap}}$	Evaporating temperature (K)
$\boldsymbol{\dot{Q}_{useful}}$	Useful heat gain (W)
$\mathbf{\dot{Q}_{total}}$	Total heat gain (W)
$\mathbf{Q_{heating}}$	Required heat for heating tap water to steady-state temperature (J)
$\mathbf{q_{design}}$	Design heating load per unit area (W/m^2)
$\dot{\mathbf{m}}$	Mass flow rate (kg/s)
$\mathbf{c_p}$	Heat capacity of fluid (J/kg. K)
$\Delta\mathbf{Tlm}$	Log-mean temperature difference(K)

1. Introduction

Environmental energy sources—such as the sun, earth, air, and water—are set to become the foundation of future heating systems. Over the past decades, new technologies have been integrated into buildings to harness these sustainable energy sources. Among them, Active Solar Thermal Facades (ASTFs) have emerged as a promising solution. ASTFs function as components of the building envelope, incorporating solar collection devices that can be linked to various energy systems (Zhang et al., 2015). This allows them to serve dual purposes, such as providing Domestic Hot Water (DHW) as well as Space Heating and Space Cooling.

A Dutch façade company, Aberson, came up with an idea that installs water tubes behind their facade products "A-Brick" (a ventilated ceramic facade system), to collect solar energy or extract heat from ambient air for heating and cooling demand. This idea is coherent to the concept of ASTF. Aberson wants to develop the concept further and make it a marketable product.

However, ASTFs are typically designed using glass or metal facades. Aberson's concept—installing water tubes behind a ceramic cladding system—lacks precedent in both commercial products and academic research. The performance, feasibility, and integration potential of making A-Brick system into ASTF remain unverified and underexplored.

Regarding these challenges, this paper aims to answer following research questions:

"In what ways can Aberson's A-Brick façade be developed into an effective Active Solar Thermal Façade (ASTF), and how effective is the system's thermal performance when integrated with different building energy systems?"

The following sub-questions are answered in the sections 3, 4, 5 and appendix: *'How can A-brick products be engineered as an ASTF?'*, *'Which key thermal properties govern the performance of the A-Brick ASTF, and what factors influence them?'*, *'How is the ASTF thermal performance when applying on different energy systems? ' 'What is the feasibility of the technical design and assembly of the A-Brick ASTF product?'*. The research report ends with sections 6 and 7 which cover the discussion, conclusion.

2. Methodology

This research combines literature review, laboratory prototype experiments, software simulations, numerical calculations and technical design **(Figure 1)**. The literature review establishes the theoretical foundation for developing the A-Brick system into an ASTF and identifies potential energy-system integration schemes.

Laboratory experiments using an A-Brick prototype, together with ANSYS CFD simulations, are conducted to evaluate thermal performance and derive key parameters for subsequent analysis. Numerical calculations assess the feasibility and effectiveness of the ASTF in real applications, while TRNSYS simulations estimate seasonal system performance. Finally, the technical design phase explores assembly feasibility through Rhino modelling, demonstrating installation options for different building scenarios and providing detailed technical drawings.

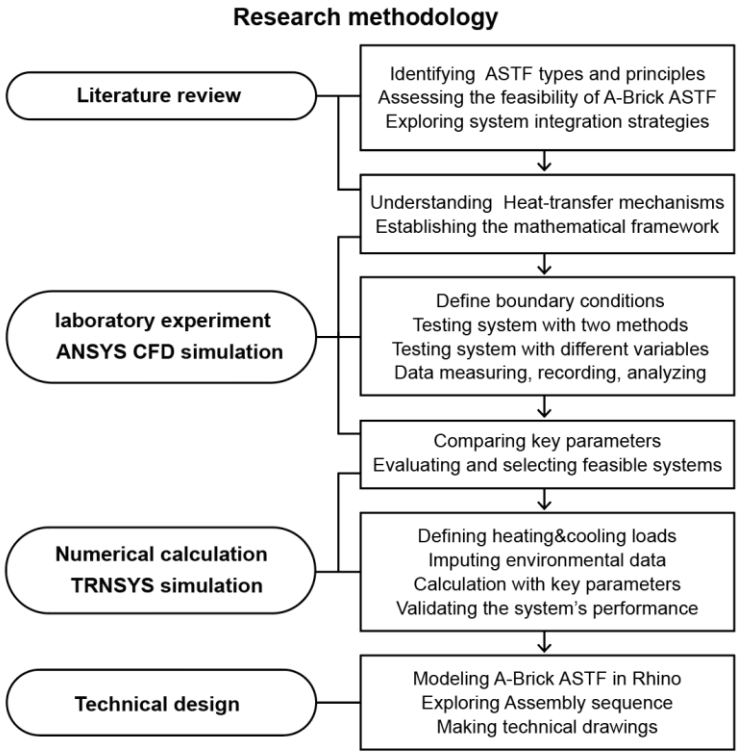

Figure 1: Research methodology framework. By author

3. A-Brick ASTF system concept

3.1 The potential of Aberson's A-Brick system

There are different types of Active solar thermal façade (ASTF) in different building parts (wall, window, balcony), heat-transfer medium (air, hydraulic, PCM, etc.) and collecting typologies (evacuated tube, glazed, unglazed, massive)(Zhang et al., 2015). Wall-type ASTF have a great advantage in that they are easier to manufacture and install. It significantly reduces construction time by enabling off-site prefabrication and rapid on-site installation, while their standardized components make it easy to replace individual units, thus enhancing maintenance.

Figure 2: Aberson's A-Brick ventilated facade system. Source: Aberson's website, https://www.aberson.nl/producten/gevelsystemen/a-brick/

Aberson's A-Brick system **(Figure 2)**, which is a new ventilated ceramic facade system, has great potential to be developed as a wall-type, water-based, unglazed ASTF. The convenience of installation and modularity of A-Brick system offer significant potential to develop it as a modular wall-based ASTF solution.

A-Brick system is composed of ceramic strips, metal cassettes, and wooden keels. The ceramic strips, in size of 300mm *75mm*20mm, are outside layers which serve as the raincoat. Metal cassettes are supporting structures which have hooks and barbs on them to secure the ceramic strips in place. Installation is straightforward: the ceramic strip is lowered onto the hook via its groove and then pressed at the top until it locks into the barb. This simple installation allows for quick assembly and easy removal, which is advantageous for ASTF integration and maintenance.

The metal cassette is 1mm thick and provides a 20mm offset, forms a cavity space backside. The wooden keels are the structure holding metal cassettes to the wall. The wooden keels, 30 mm thick, support the cassettes and add an additional cavity between each structural element. Together, the cassette and keel create a total cavity depth of 50 mm, offering suitable space for ASTF engineering.

3.2 Heat collector and heat exchangers

The idea of converting A-Brick system into an ASTF system is to integrate water tubes behind the ceramic cladding, allowing the façade to actively exchange heat with the outdoor ambient air. The A-Brick ASTF system is able of operating in 2 different modes **(figure 3)**. It can operate as a heat exchanger, where the circulating water removes indoors heat and releases it to the outside, or conversely, extracts outdoor heat and provides indoor heating. It can also act as a solar collector when the façade is oriented toward the sun. In this way, the A-Brick ASTF essentially functions as a specialized heat exchanger that the ceramic surface absorbs solar radiation and transfers the energy to the water in the tubes.

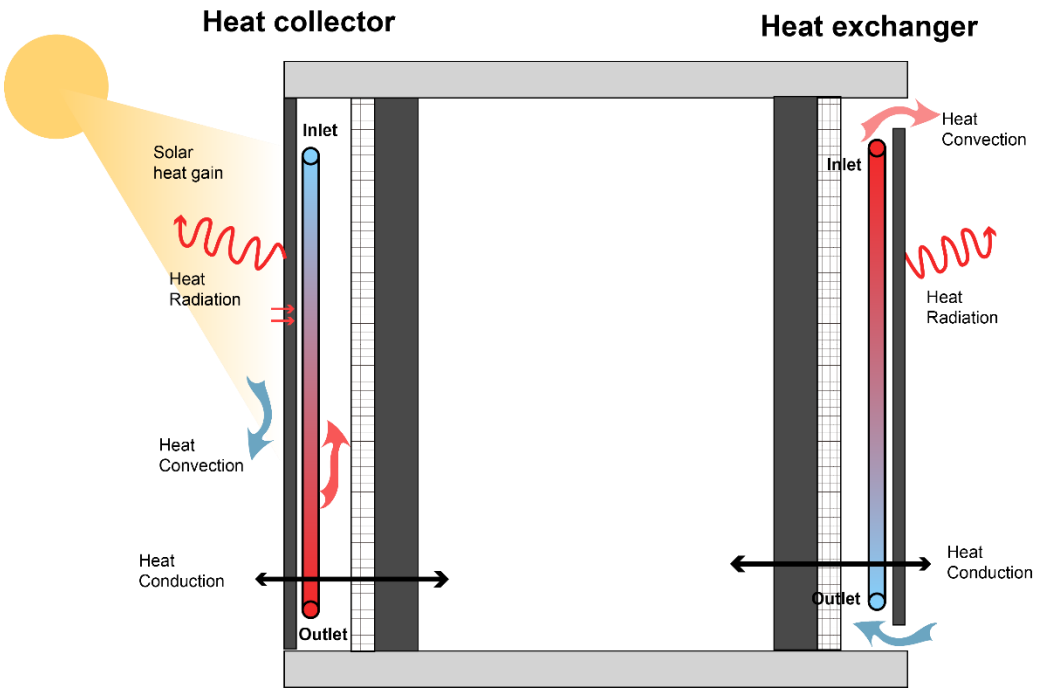

Figure 3: Two operating modes of A-Brick ASTF system. *By author*

A-brick system that serves as ASTF has several advantages. For heat exchangers, the ceramics are not tightly bonded; the tiny gaps promote air convection between cavity air and outdoor air, increasing heat exchanger efficiency. And the moderate thickness (20mm) makes it easier conducting heat between outside and inside surface. As a heat collector, the high heat capacity of ceramic enabling thermal storage effect, providing stable heat source.

Another advantage of A-Brick ASTF system is when applying on a heat pump system, it replaces conventional outdoor fan coil unit **(figure 4)**, serve as an intermediary heat exchanger between the external environment and the heat pump refrigerant circuit, which not only promoting thermal performance by increasing heat exchanging surface area but also enhancing aesthetic feelings of the building's appearance by cancelling outdoor fan unit.

Figure 4: Replacement of outdoor fan unit. *By author*

3.3 Possible energy systems

About two-thirds of household energy goes to space heating (roughly 63.5% in the EU) and around 17% to domestic hot water (DHW) (Kamps, 2023). A-Brick ASTF can be used for both space heating, space cooling and domestic hot water production. It can be used either as a solar collector for low temperature heating or as a heat exchanger connected with multifunctional heat pumps. In the following part, we will discuss the application of A-Brick ASTF in 1) low temperature heating 2) combination with heat pump

3.3.1 low temperature heating application

While integration with heat pumps unlocks higher-temperature potential, the A-Brick ASTF system exhibits inherent strengths for direct, low-temperature thermal energy collection. Its ceramic cladding and operational characteristics make it particularly well-suited for applications requiring modest temperature lifts above ambient.

1) DHW preheating

Using A-Brick ASTF for DHW preheating -raising inlet water from 10°C to 25-35°C- substantially reduces the energy required by the primary heater to reach the final set point (usually 55-60°C), improving overall system efficiency and reducing operating costs.

In a typical configuration **(figure 5)**, the water loop connected to the A-Brick ASTF absorb heat from the façade collector and transfers it into a water tank. Cold tap water in the load loop passes through this tank, where it is preheated before entering an auxiliary heater (boiler or heat pump) to reach the required DHW temperature. A smart-controlled pump should be used to operate a source loop only when solar heat is available.

Under favourable solar conditions, A-Brick ASTF panels can deliver outlet water temperatures in the range of 30–40 °C on clear days, with performance decreasing as cloud cover increases. However, in Dutch winters, low solar altitude, limited irradiance, and cold ambient air significantly reduce heat output. Therefore, a conventional heater is required year-round to ensure reliable hot water supply.

With moderate Dutch sun, an ASTF on the south facade could supply a significant fraction of summer DHW heat, but only a minority of the annual demand. For example, O'Hegarty et al. (2015)find that 168 m^2 of collectors plus ~6000 L of storage were required to cover 25% of an apartment block's DHW load. Conversely, a small-scale facade (e.g. 4 m^2) could cover ~50–60% of a modest home's DHW in sunnier summer months (Zhang et al., 2015). In practice, a well-designed ASTF/DHW system might replace 20–40% of annual water heating energy for typical use, mostly in spring/summer; fall/winter yield is much lower.

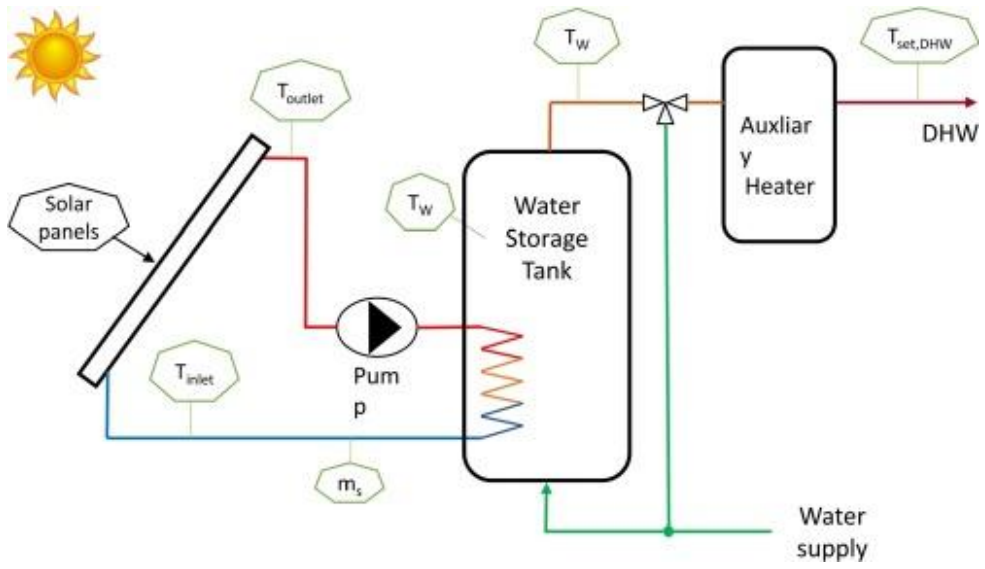

Figure 2: Scheme of the DHW preheating system.
Reprinted from "*Analysis of the performance of a building solar thermal facade (BSTF) for domestic hot water production*" by Gagliano et al. (2019). *Renewable Energy*, *142, 511–526. https://doi.org/10.1016/j.renene.2019.04.102*

2) Swimming pool heating

Swimming pools are commonly used in many residential and holiday homes. There are both indoor and outdoor pools. While outdoor pools are mainly used during summer, indoor pools are used all year around. Swimming pools are usually heated to temperatures above the ambient air. For indoor pools, the ideal water temperature is generally between 28°C and 31°C (Dannemand et al., 2025) .

An A-Brick ASTF could serve as an auxiliary pool heater. It won't replace conventional heating (or heat pump) but can significantly reduce energy use during peak season. With ASTF, one would typically run through a closed glycol loop through the facade and transfer heat to the pool via a plate of HX (to avoid corrosion from pool chemicals). Simple control diverts flow to the pool loop when solar heat is sufficient. Unlike DHW, the pool itself is a large thermal mass that acts as storage.

In summer, ASTF can substantially extend the swimming season or raise the temperature. For example, solar pool heating "is cost-effective" because it uses large-area collectors at low temperature. A facade area of e.g. 20–30 m^2 facing south could provide on the order of several kW of heat on sunny days, offsetting part of pool heating (Chow et al., 2012).

Practically, ASTF pool heating is seasonal. It works best from late spring to early fall.(Li et al., 2023) When daylight is plentiful, the facade can preheat pool water each day; at night or in winter, the pool will cool rapidly, and a secondary heater is needed (gas or electric). If the pool is covered when not in use, a modest ASTF system can maintain its temperature when it is sunny.

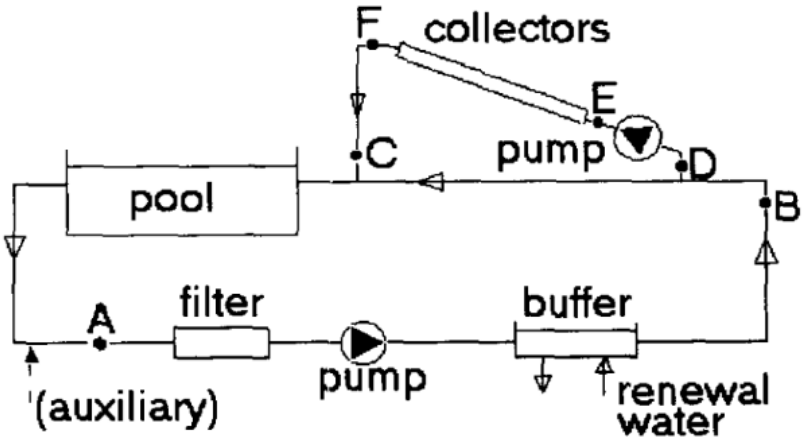

Figure 3: Schematic diagram for pool heating system
Reprinted from "*Thermal analysis of five outdoor swimming pools heated by unglazed solar collectors*" by Molineaux et al. (1994). *Solar Energy, 53(1), 21–26. https://doi.org/10.1016/s0038-092x(94)90599-1*

3.3.2 Integration with heat pumps

1) Integration with Indirect Solar-Assisted Heat Pump (IDX-SAHP)

Integrating solar collectors and heat pumps to form a solar assisted heat pump (SAHP) system has been widely applied in DHW producing and space heating(Buker & Riffat, 2016). This system allows the heat pump to operate with a relatively higher temperature solar water source than traditional air source heat pump, resulting in improved COP and enhanced overall system efficiency.

Solar assisted heat pump can be categorised in two types, Direct SAHP and In-Direct SAHP. In the DX-SAHP, the refrigerant directly flow through solar collector then evaporates after heated by the solar radiation (Kuang & Wang, 2006) Given that the A-Brick ASTF system is not specifically engineered to handle refrigerants or the associated pressures, it is not suitable for use as an evaporator in a DX-SAHP configuration.

Instead, its optimal application is within In-direct SAHP systems, where it can efficiently preheat a secondary fluid that then transfers heat to the heat pump, enhancing overall system performance (Wang et al., 2017). In this setup, the water-glycol run through the solar collector and absorb solar energy, then it exchanges heat with refrigerant at a heat-exchanger. The heat exchanger is function as an evaporator.

The thermal efficiency of ASTF solar collector systems depends on several critical parameters, with ambient temperature and fluid inlet temperature emerging as the most influential factors affecting overall performance (Elguezabal et al., 2020). Elguezabal et al conduct at an experimental building in Derio, Spain, evaluated an 18 m^2 ASTF which installed 6 metal absorber panels connected to a

6 kW heat pump **(Figure 7).** In a summer day, it represents a total daily DHW production of 46.7 kWh and a maximum COP of 4.77.

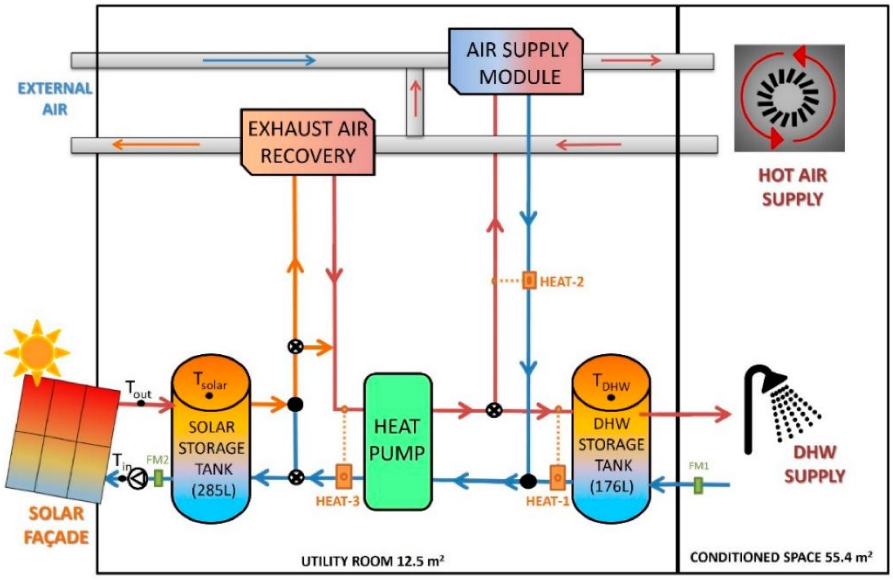

Figure 7: Schematic of combined ASTF+ heat pump system

Reprinted from "*Assessment on the Efficiency of an Active Solar Thermal Facade: Study of the Effect of Dynamic Parameters and Experimental Analysis When Coupled/Uncoupled to a Heat Pump*" by Elguezabal et al. (2008). *Energies, 13(3), 597. https://doi.org/10.3390/en13030597*

2) Integration with Multifunctional Heat Pumps

Multifunctional Heat Pump system is a complex system that enables triple functions which are space heating, space cooling and DHW producing. The implementation of A-Brick ASTF in multifunctional Heat Pump replaces traditional outdoor fan coil unit, serve as a heat exchanger between the external environment and the heat pump refrigerant circuit.

Several research have been conducted with different Multifunctional heat pumps, including Multifunctional Air Source Heat Pump (ASHP), Multifunctional SAHP, Air conditioning water heater, etc.

Fan (2019) have come up with a multi-functional air source heat pump water heater system. The system enables cooling, heating, and hot water production. A four-way reversing valve makes it possible to switch between cooling and heating modes. When this system is combined with an A-Brick ASTF, the air heat exchanger is replaced by an ASTF water loop and a water-to-water heat exchanger.

Amin & Hawlader (2013) produced an multifunctional SAHP system in Singapore **(Figure 8)**. The indoor evaporative fan coil and outdoor solar collector were connected in parallel. The outdoor air coil condenser and heat storage condenser were connected in series. The maximum COP of the system can reach up to 8.

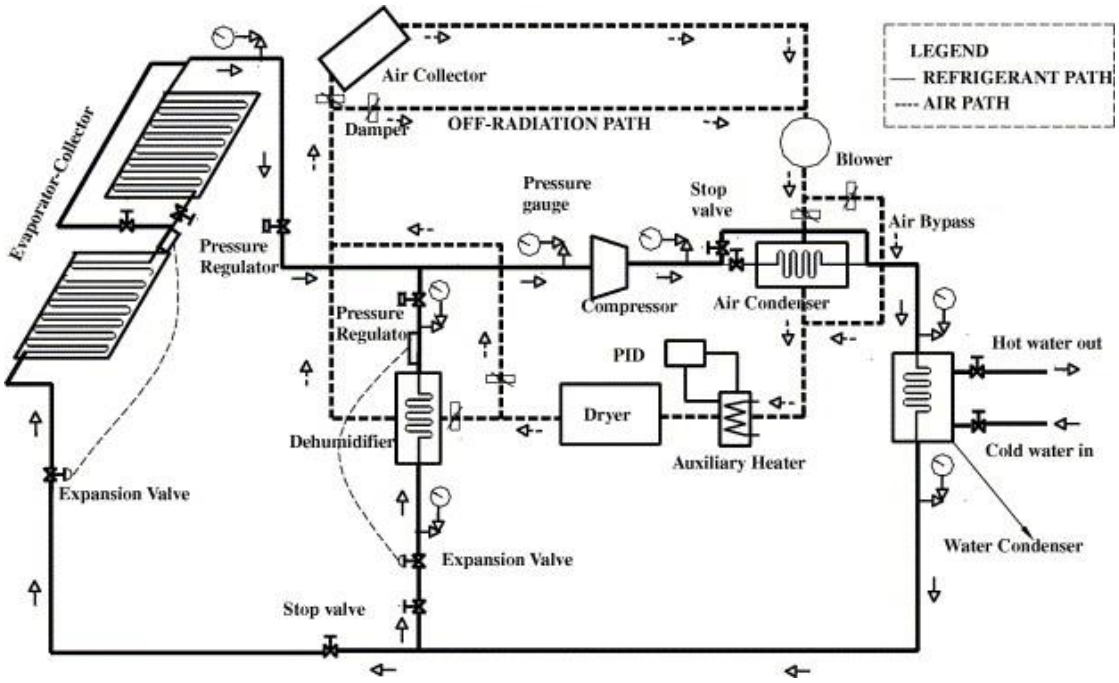

Figure 8: Schematic diagram of an integrated solar heat pump system.
Reprinted from "*A review on solar assisted heat pump systems in Singapore*"
by Amin, Z. M., & Hawlader, M. (2013). *Renewable And Sustainable Energy Reviews, 26, 286-293. https://doi.org/10.1016/j.rser.2013.05.032*

4. A-Brick ASTF's thermal properties

In the previous chapter, the possibility of connecting A-brick ASTF with various systems was explored. However, performance of these systems ultimately depends on the ability of ASTF to transfer heat. Therefore, this chapter focuses on analyzing the heat transfer capability of the A-Brick ASTF system in both heat collector and heat exchanger modes. Through a series of experimental model testing and software simulations, the aim is to measure key parameters—collector efficiency, heat removal factor and overall heat loss coefficient—that determine the system's effectiveness. These results will serve to assess the suitability of A-Brick ASTF in different energy applications in next chapter.

'Which key thermal properties govern the performance of the A-Brick ASTF, and what factors influence them?

4.1 Laboratory prototype experiment setup

The experiment to evaluate A-Brick ASTF thermal properties is conducted in indoor environments by both steady-state and transient methods. The indoor condition consideration fixes the solar radiation, ambient temperature, wind velocity, and background radiation, to improve the experimental uncertainty.

A prototype of A-Brick product from Aberson company (0.6m× 1m) is used to reproduce realistic façade conditions **(figure 9)**, which consists of ceramic claddings mounted on two metal cassettes, and they are fixed on a supported backplate by wooden keels.

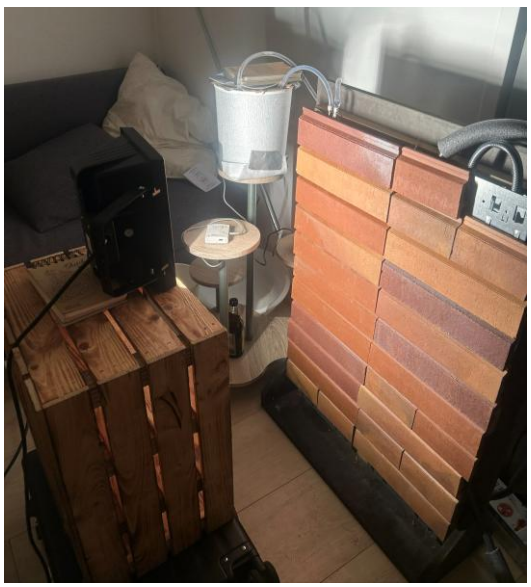

Figure 9: A-Brick prototype.
By author.

Figure 10: Experiment instruments.
By author.

Aa adjustable halogen lamp (0 to 2000W) is used as the solar heating source; the value is measured by a solar power meter. A 5W water pump is used to drive the water circulate in the ASTF and both inlet and outlet water temperature, as well as air temperature, are recorded by two data loggers. An infrared thermometer is used to measure ceramic's surface temperature **(figure 10).**

There are Four configurations applied in the experiment, which have different pipe materials and pipe positions **(figure 11)**. Two configurations that water pipes are in between ceramic claddings and in front of metal cassette are mainly applied in thermal collector experiments, including PVC-front and steel-front. While other two configurations that water pipes are in the air cavity and back of the metal cassette are mainly applied in thermal exchanger experiments, including cooper-back and steel-back configurations.

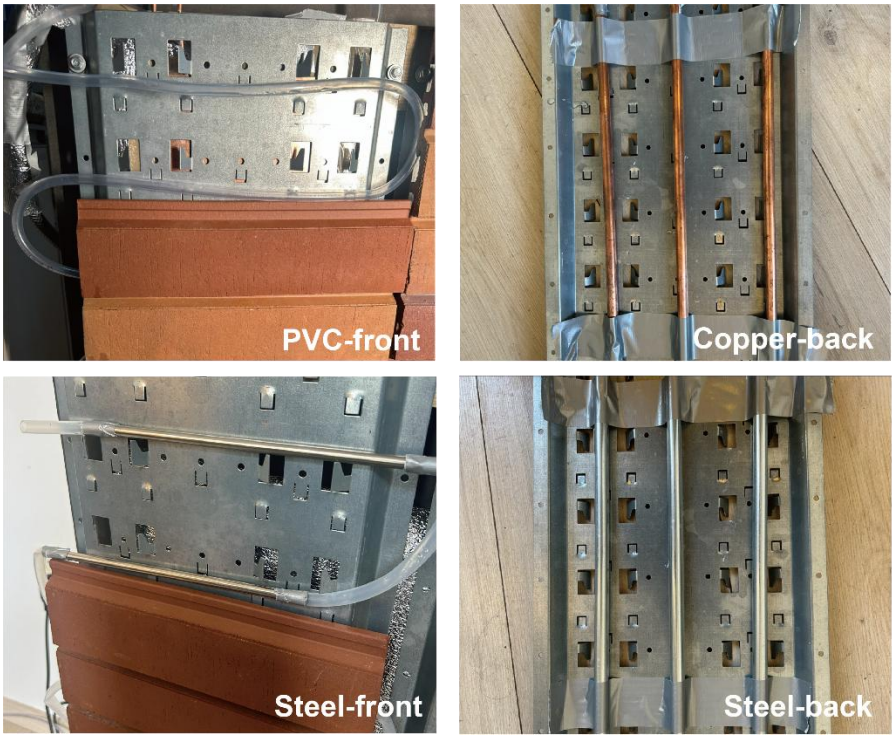

Figure 11: Four different experiment configurations. *By author.*

Two methods are applied in model test, including steady-state method and transient method **(figure 12)**. For steady-state method, water flows in an open circuit. Different temperatures of tap water flow into the inlet then flow out from outlet. Two temperature data loggers are placed both at water inlet and outlet to measure the temperature difference. For transient method, water flows in a closed circuit. A certain amount of water is placed in an insulated water tank, and the water is continuously circulated in ASTF, driven by a water pump in water tank. The probe of temperature data logger is placed in the tank to measure water temperature rise over time.

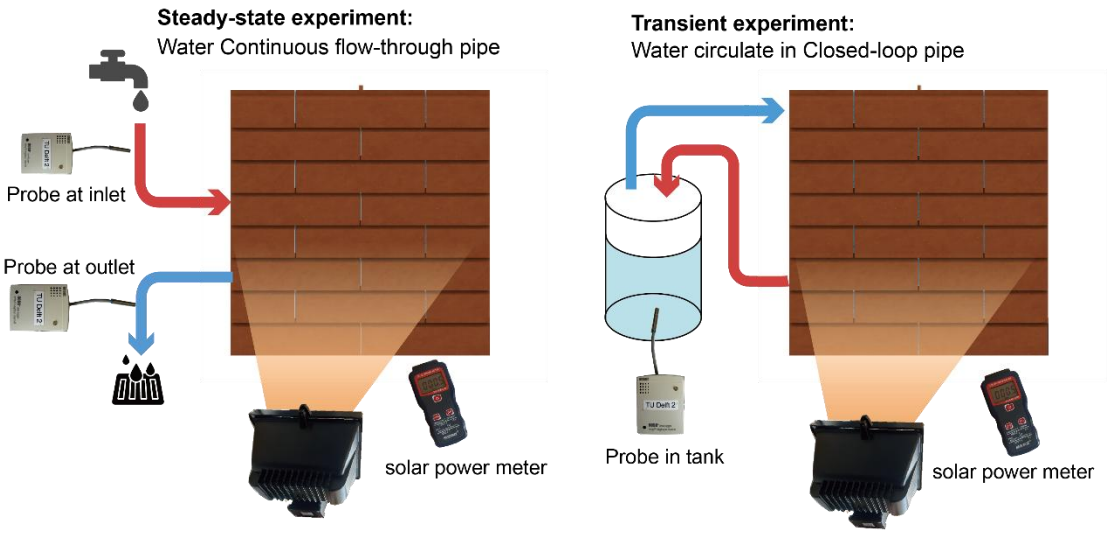

Figure 12: Steady-state method and transient method explanation. *By author.*

4.2 Results of Heat collector

4.2.1 Heat collector energy balance

A solar collector is a specialized heat exchanger that converts solar radiation into usable thermal energy. When A-Brick ASTF is used as a heat collector, the useful heat gain can be described by the standard energy balance equation for solar collectors, as shown in **Equation (1)** (Duffie & Beckman, 2013). It describes in steady state, the useful energy gains are equals the difference between absorbed solar energy and thermal loss to the environment.

$$\dot{Q}_{total} = GA(\tau\alpha) - h_L A\left(T_{pl} - T_a\right) \tag{1}$$

Where:

G: Solar irradiance (W/m²)

$\boldsymbol{\tau\alpha}$: Transmittance and absorptance of the surface ($\tau\alpha \approx 0.8$ for dark ceramic)

$\mathbf{h_L}$: Overall heat-loss coefficient (W/m²K)

A: ASTF surface area (m²)

$\mathbf{T_{pl}}$: Absorber Plate (ceramic claddings) temperature (K)

$\mathbf{T_a}$: Ambient air temperature (K)

This is the heat balance equation for ideal situation when the collector's temperature is equal to the inlet fluid temperature. But in actual working conditions, there is heat loss due to the temperature difference between wall plate and collector-inlet temperature. So, it needs to introduce heat removal factor $\mathbf{F_R}$ to measure how effectively the circulating fluid removes the absorbed solar heat from the collector compared with an ideal case where the collector's absorber plate is always at the inlet fluid temperature(Duffie & Beckman, 2013).

$$F_R = \frac{\dot{Q}_{useful}}{\dot{Q}_{total}} \tag{2}$$

$$\dot{Q}_{useful} = A \times F_R \times [G(\tau\alpha) - h_L(T_{in} - T_a)] \tag{3}$$

Where:

$\dot{Q}_{useful}$: Useful heat gain (W)

$\dot{Q}_{total}$: Total heat gain (W)

F_R: Heat removal factor

T_{in}: Inlet fluid temperature (K)

Equation (3) is a widely used relationship for measuring collector energy gain and is generally known as the "Hottel-Whillier-Bliss equation"(Duffie & Beckman, 2013).

To measure the performance of solar collectors, collector efficiency is introduced. According to Duffie & Beckman, the definition of collector efficiency is the ratio of useful heat output of the collector to the total solar energy incident on its surface. **Equation (4)** expresses how effectively the incoming solar energy is converted into useful thermal energy in the working fluid. This metric enables comparison between different A-Brick ASTF materials and configurations, as well as benchmarking the A-Brick ASTF against conventional flat-plate collectors.

$$\eta = \frac{\dot{Q}_{useful}}{GA} \tag{4}$$

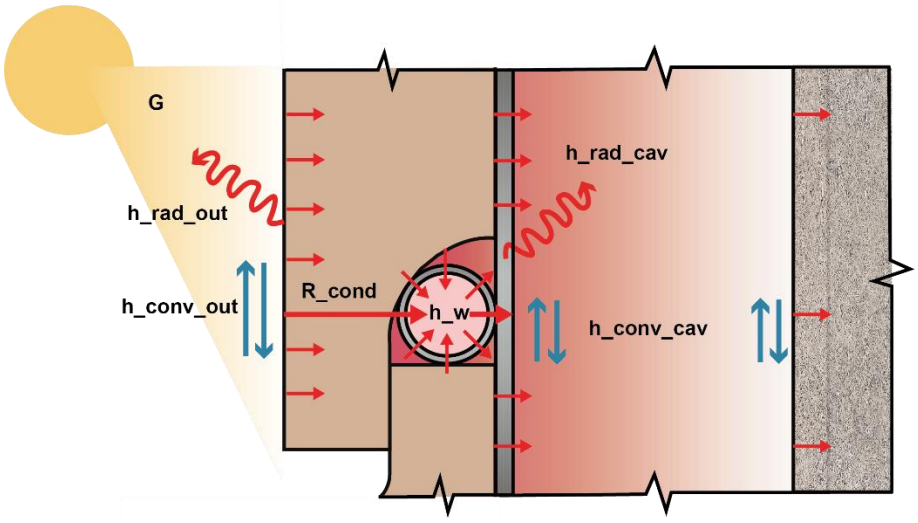

Figure 13: Heat path diagram in solar collector mode. *By author.*

4.2.2 Results of steady-state prototype experiments

The objective of the steady-state experiment is to determine the collector efficiency $\boldsymbol{\eta}$, heat-removal factor $\mathbf{F_R}$, and overall heat-loss coefficient $\mathbf{h_L}$, which can then be compared with the performance of conventional flat-plate collectors. In this test, water circulates through an open-loop system while the inlet and outlet temperatures are monitored until steady thermal equilibrium is achieved. Once the system reaches steady state, the useful heat gains $\boldsymbol{\dot{Q}_{useful}}$ is calculated using the following expression:

$$\dot{Q}_{useful} = \dot{m} \times Cp \times (T_{out} - T_{in}) \tag{5}$$

Where:

$\boldsymbol{\dot{m}}$: Mass flow rate (kg/s)

$\mathbf{c_p}$: Heat capacity of fluid (J/kg. K)

$\mathbf{T_{out}}$: Fluid outlet temperature (K)

$\mathbf{T_{in}}$: Fluid inlet temperature (K)

Several prototype experiments have been conducted with identical configuration (PVC- front) and mass flow rate (10kg/h). Three sets of experiments with different solar heating powers (600W/800W/1200W) were conducted, with 5 different inlet water temperatures, allowing for linear fitting of the results. The inlet/outlet temperature, indoor environment temperature and collector efficiency data are shown in **Table1** and **Figure 14.**

Table 1

Measured temperatures and collector efficiency under different solar powers

Solar power	T_{in}	T_{out}	T_a	η
600W	16.6	17.9	22.6	0.28
	17.8	18.9	22.2	0.24
	19.2	20.1	22.8	0.19
	20.5	21.4	22.5	0.19
	23.0	23.8	22.5	0.17
800W	13.9	15.7	23	0.29
	17.0	18.6	23.4	0.26
	21.7	22.9	23.5	0.19
	25.3	26.3	22.5	0.16
	29.1	29.7	22.5	0.10
1200W	16.8	19.6	23.5	0.26
	23.1	25.6	23.5	0.23
	26.1	28.3	24	0.20
	30.4	32.1	22.5	0.16
	35.9	36.7	23.5	0.07

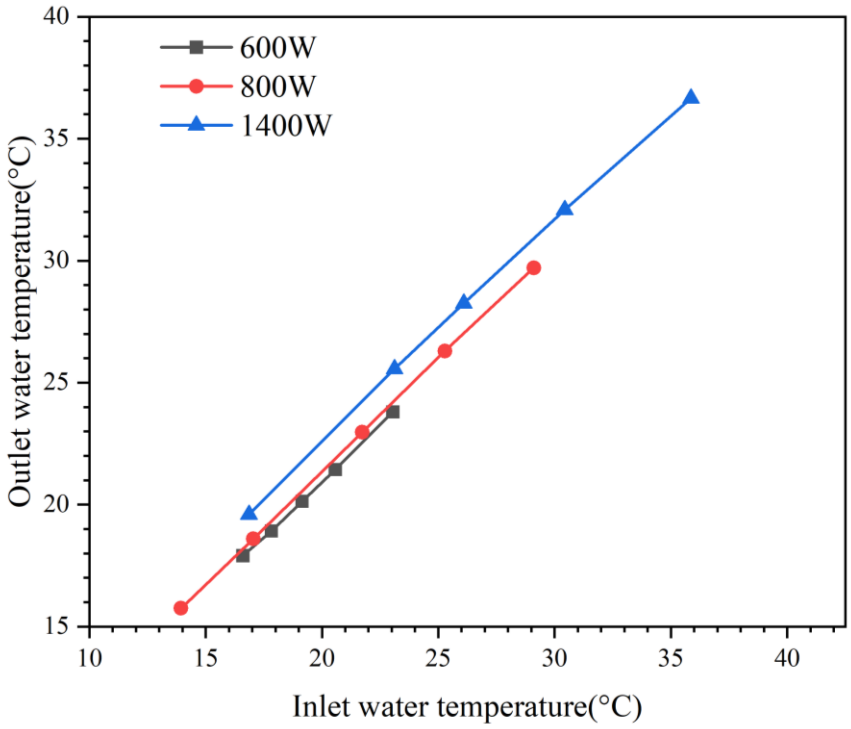

Figure 14: Inlet and outlet water temperatures under different solar heating powers. *By author.*

By combining **Equation (3)** and **(4)**, we can calculate the $\mathbf{F_R}$ and $\mathbf{U_L}$ by collector efficiency **Equation (6)**:

$$\eta = \frac{\dot{Q}_{useful}}{GA} = F_R(\tau\alpha) - F_R h_L \frac{(T_{in} - T_a)}{G} \tag{6}$$

This is linear regression equation. It can be represented as

$$Y = ax + b$$

While

$$Y = \frac{Q_{useful}}{GA}, \quad X = \frac{(T_{in} - T_a)}{G}, \quad a = -F_R h_L, \quad b = F_R(\tau\alpha)$$

Slope a $\boldsymbol{(-F_R h_L)}$ is the factor of collector heat losses due to environment effect, while the interception b $(\boldsymbol{F_R(\tau\alpha)})$ is the fraction of the solar radiation gains.

By applying linear regression to the experimental data, the results are shown in **Figure 15**. The regression lines corresponding to the three solar heating powers (600 W, 800 W, and 1200 W) almost collapse onto one another, exhibiting very similar slopes and intercepts. This indicates that the heat removal factor, $\mathbf{F_R}$, remains essentially constant when the mass flow rate is fixed, regardless of the applied irradiance level.

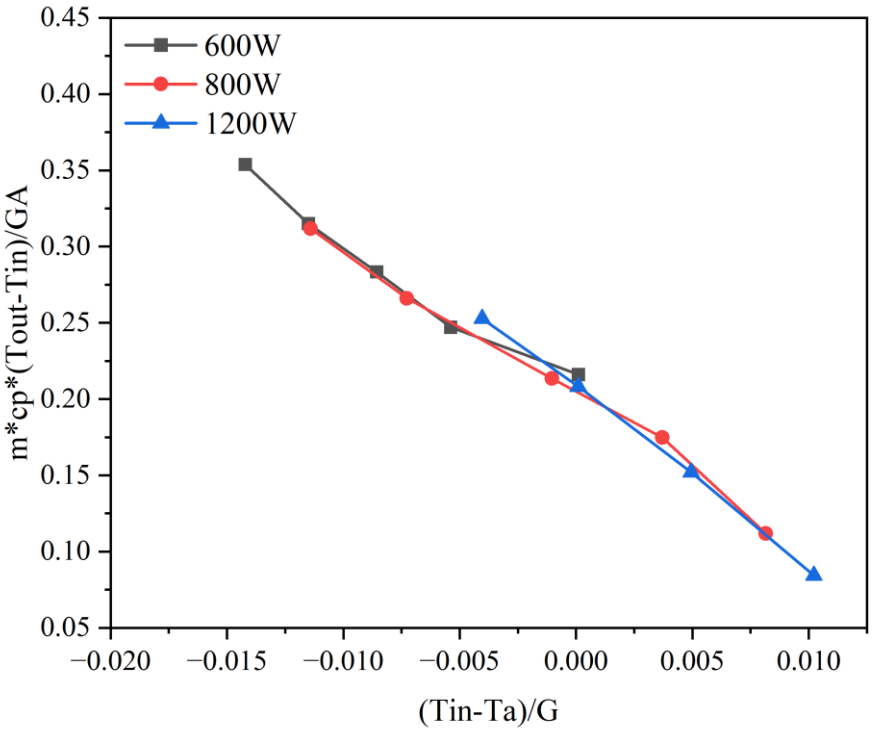

Figure 15: Nondimensional performance curves showing the relationship between $(T_{in} - T_a)/G$and $mc_p(T_{out} - T_{in})/GA$ for three solar heating powers. *By author.*

The fitted coefficients are:
Slope: $a = F_R h_L = -11.02\,\mathrm{W/m^2.°C}$
Intercept: $b = F_R(\tau\alpha) = 0.21$

Given that the ceramic surface is dark colored with an effective absorptance of approximately $(\tau\alpha) = 0.80$, the heat removal factor and overall loss coefficient can be calculated as:

$$F_R = \frac{b}{(\tau\alpha)} = 0.26$$

$$h_L = \frac{a}{F_R} = 41.6\,\mathrm{W/m^2.°C}$$

These values are consistent with the expected performance of a ventilated ceramic façade collector, where the back cavity and ceramic thermal resistance contribute to moderate heat removal efficiency and a relatively high overall heat-loss coefficient.
To contextualize the measured performance of the A-Brick ASTF, its heat removal factor $\mathbf{F_R}$ and heat-loss coefficient $\mathbf{h_L}$ are compared with typical values reported

for other collector types. A summary of representative ranges is provided in **Table 2**.

Table 2

Comparison of thermal performance parameters for different collector types

Collector type	F_R	h_L	η
A-Brick ASTF	0.25-0.35	35–45	15–30%
Metal-based ASTF	0.45–0.65	10–20	35–55%
Flat-Plate Collector	0.70–0.85	3–8	50–70%
Evacuated Tube Collector	0.85–0.95	1–2	60–75%

Note. Data for flat-plate and evacuated tube collectors from Duffie & Beckman (2013); metal-based ASTF from (Elguezabal et al., 2020)

4.2.3 Results of transient prototype experiments

Transient experiments evaluate the dynamic response of the A-Brick collector, including steady-state temperatures $T\infty$ and time constants τ under varying conditions. A closed-loop system with a fixed water volume (1 L) is used. Temperature rise in the insulated tank is monitored over time. Three variables were tested:

1) Irradiance

With same configuration (PVC-front) and mass flow rate (10kg/h), increasing lamp power (400–1500 W/m^2) results in proportionally higher steady-state water temperatures. **(Figure 16)**

2) Mass flow rate

At identical irradiance (1200 W/m^2) and configuration (PVC-front) increasing mass flow rate from 10kg/h to 60 kg/h results in similar steady-state temperature but faster respond time, indicating that flow rate mainly affects dynamic behaviour rather than final equilibrium. **(Figure 17)**

3) Configuration

With equal irradiance (1200W/m2) and flow rate (10kg/h), different configurations show distinct steady-state temperatures due to variations in pipe material and position. **(Figure 18)**

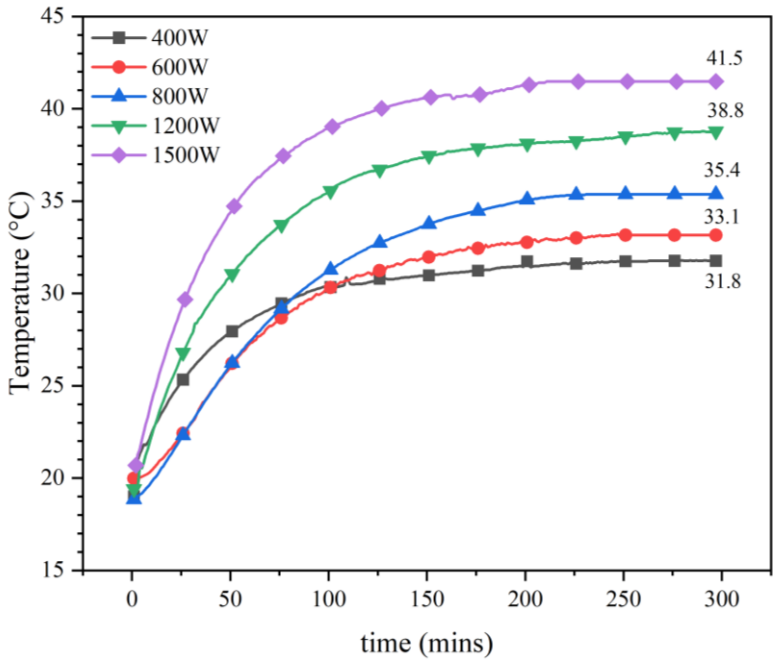

Figure 16: Transient water temperature response under different irradiance levels for the PVC-front configuration at 10 kg/h mass flow rate.

Note. Higher irradiance produces proportionally higher steady-state temperatures. *By author*

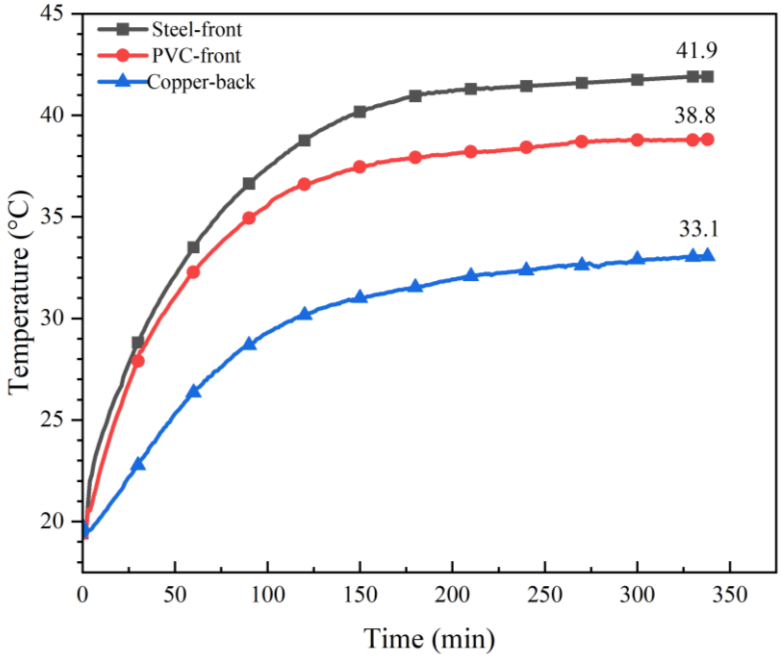

Figure 17: Transient water temperature response under different ASTF configurations at 1200 W/m^2 heating power and 10 kg/h mass flow rate.

Note. Configurations differ in pipe material and position. *By author*

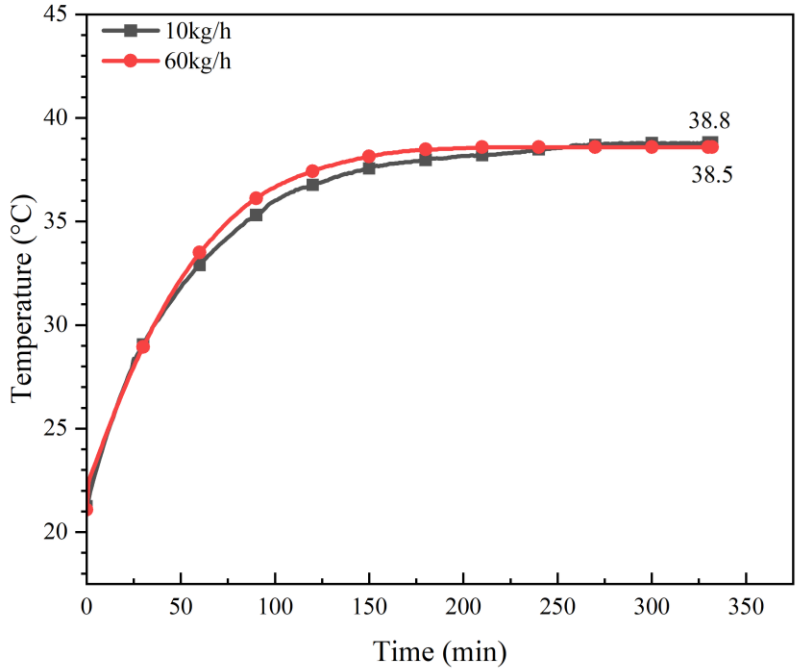

Figure 18: Transient water temperature response under different mass flow rates at 1200 W/m^2 irradiance for the PVC-front configuration.

Note. Higher flow rate yields faster thermal response while steady-state temperature remains similar. *By author*

Different configurations also result in different respond time. To quantify response speed, the temperature-time curve is fitted using the first-order exponential model by **Equation (7)**.

$$T(t) = T_\infty - (T_\infty - T_0)e^{-t/\tau} \tag{7}$$

Time constant $\boldsymbol{\tau}$ describes how fast the system reacts to heating process. $\mathbf{t}$ is heating time. $\boldsymbol{T_0}$ is initial water temperature. The time constant $\boldsymbol{\tau}$ can be obtained from the slope of the linearized form.

$$\ln\big(T_\infty - T(t)\big) = \ln(T_\infty - T_0) - \frac{t}{\tau}$$

A smaller time constant $\boldsymbol{\tau}$ means the system responds faster. Results in **Figure 19** show that Steel-front has the smallest $\boldsymbol{\tau}$ (fastest response), while Copper-back exhibits the largest $\boldsymbol{\tau}$ (slowest heat-up), reflecting the influence of pipe placement and material conductivity.

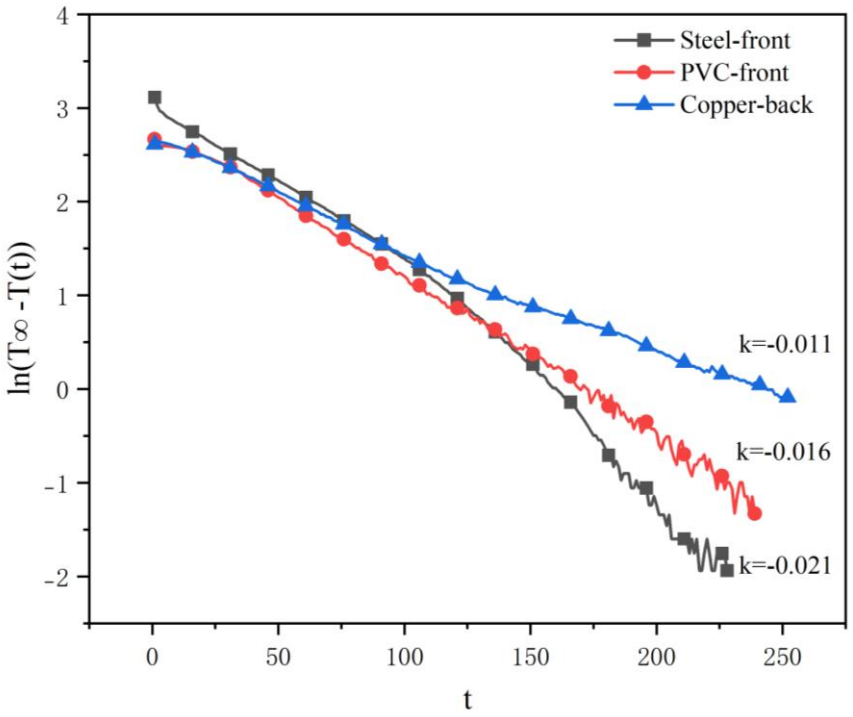

Figure 19: Linearized transient response ln (T∞ − T(t)) for estimating time constants under different ASTF configurations at 1200 W/m^2 irradiance and 10 kg/h flow rate.

Note. Time constant τ is obtained from the slope of ln (T∞ − T(t)) = ln (T∞ − T_0) − t/τ. *By author*

4.3 Results heat exchanger

4.3.1 Heat exchanger energy balance

When the A-Brick façade operates as a heat exchanger, the primary heat-transfer pathway differs from that of a solar collector. Because water pipe is placed at the back of the metal cassette to increase convective exchange with cavity air. The dominant mechanism is therefore the heat is released to cavity air and then conduct to ceramic cladding surface. The effective heat-exchanging surface area can be represented by interface between air cavity and ceramic claddings as same as interface between ceramic claddings and outdoor environment. Direct solar radiation is not considered in this mode, as solar irradiance is insufficient for heat extraction in winter and hinder heat releasing in summer. The useful heat exchanged can be described by the standard heat-exchanger **Equation (8)**:

$$\dot{Q} = h_{\text{sys}} A \Delta T_{\text{lm}} \tag{8}$$

Where:

h_{sys}: Overall heat-transfer coefficient

A: Effective heat-exchanging surface area

ΔT_{lm} : Log-mean temperature difference between water and ambient air. It describes the "equivalent temperature difference" when the temperature difference between two fluids along the length of a heat exchanger is not constant. ΔT_{lm} can be described by **Equation (9)**

$$\Delta T_{\mathrm{lm}} = \frac{(T_{\mathrm{in}} - T_{\mathrm{a}}) - (T_{\mathrm{out}} - T_{\mathrm{a}})}{\ln[\frac{T_{\mathrm{in}} - T_{\mathrm{a}}}{T_{\mathrm{out}} - T_{\mathrm{a}}}]} \tag{9}$$

Heat path diagram shows in **Figure 20** (in cooling mode). There are mainly three heat paths. The first path is heat is released to cavity air then exchanged to outdoor by cavity ventilation. The second path is the heat from pipe or cavity air conduct through metal cassette and ceramic, then exchanged with outdoor environment by convection and radiation. The third path is heat from cavity air conduct through insulation and structural wall then released to indoor air.

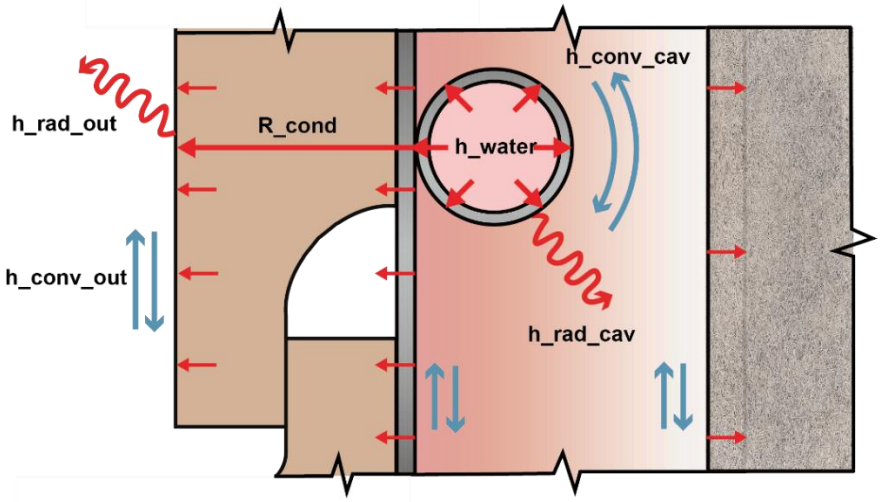

Figure 20: Heat path diagram in heat exchanger cooling mode. *By author.*

System heat-transfer coefficient $\mathbf{h_{sys}}$ integrates all conductive, convective and radiative resistances. Because these resistances depend on ambient air temperature, cavity ventilation, pipe conductivity, and water flow rate, $\mathbf{h_{sys}}$ is not constant and must be determined for different conditions. Several model tests and software simulations have been conducted to measure $\mathbf{h_{sys}}$ in different working conditions. Steady-state model tests are aimed at showing how different pipe position, pipe material and wind speed leads to different $\mathbf{h_{sys}}$. Software simulations are aimed at obtaining the $\mathbf{h_{sys}}$ in real heat pump working conditions.

4.3.2 Results of steady-state prototype experiments

In steady-state experiments, Water flows in an open circuit under controlled inlet temperatures (60°C). Once outlet temperatures stabilize, $\mathbf{h_{sys}}$ can be calculated by **Equation (5)** and **(8)**:

$$h_{\text{sys}} = \frac{\dot{m} c_{\text{p}} (T_{\text{in}} - T_{\text{out}})}{A \Delta T_{\text{lm}}}$$

1) Pipe position

Two configurations with identical pipe material (steel) but different positions (front-mounted/back-mounted) were compared in different mass flow rates, the results show in **Figure 21**.

Back-mounted pipes yield significantly higher water temperature difference and higher $\mathbf{h_{sys}}$ values compared to front-mounted configurations in collector mode. This confirms that placing pipes near the cavity side enhances heat exchange with ambient air.

2) Pipe material

Two configurations with identical pipe position (back-mounted) but different materials (steel/copper) were compared in different mass flow rates, the results show in **Figure 22**.

Copper showed higher $\mathbf{h_{sys}}$ due to its superior thermal conductivity, though the difference was moderate, indicating that air-side convection dominates the overall resistance.

3) Wind speed

An electric fan was used to generate different wind speeds for the same configuration (steel-back) and mass flow rate (60kg/h). **Figure 23** shows that Increasing wind speed caused an obvious increase in $\mathbf{h_{sys}}$, demonstrating the strong sensitivity of the façade system to cavity ventilation and external air movement.

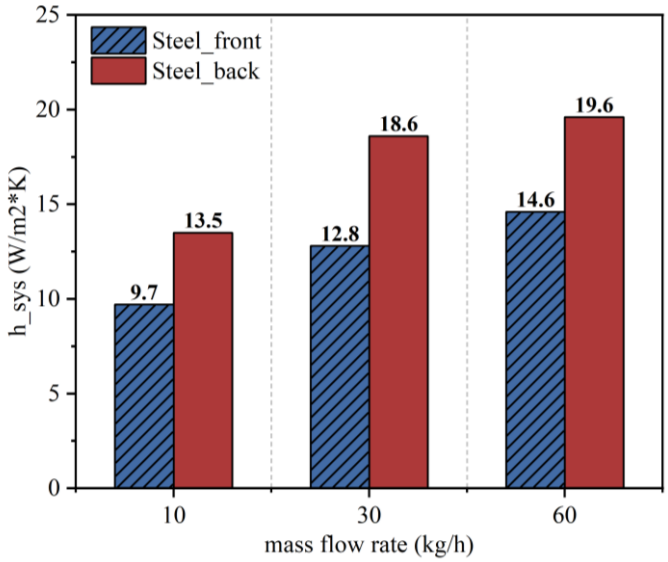

Figure 21: Effect of pipe position on $\mathbf{h_{sys}}$ at different mass flow rates.

Note. Back-mounted pipes yield significantly higher h_{sys} due to enhanced heat exchange on the cavity side. *By author*

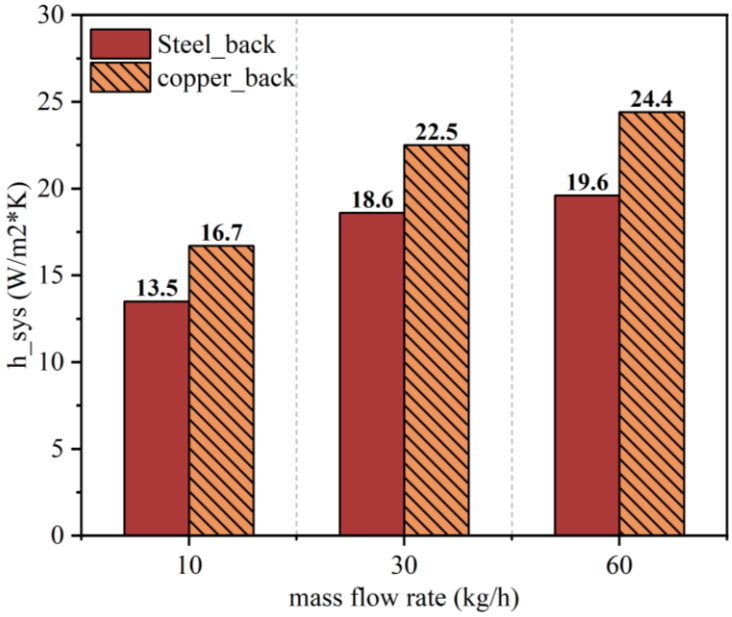

Figure 22: Effect of pipe material on $\mathbf{h_{sys}}$ at different mass flow rates.

Note. Copper pipes show higher h_{sys} owing to higher thermal conductivity, though air-side convection remains dominant. *By author*

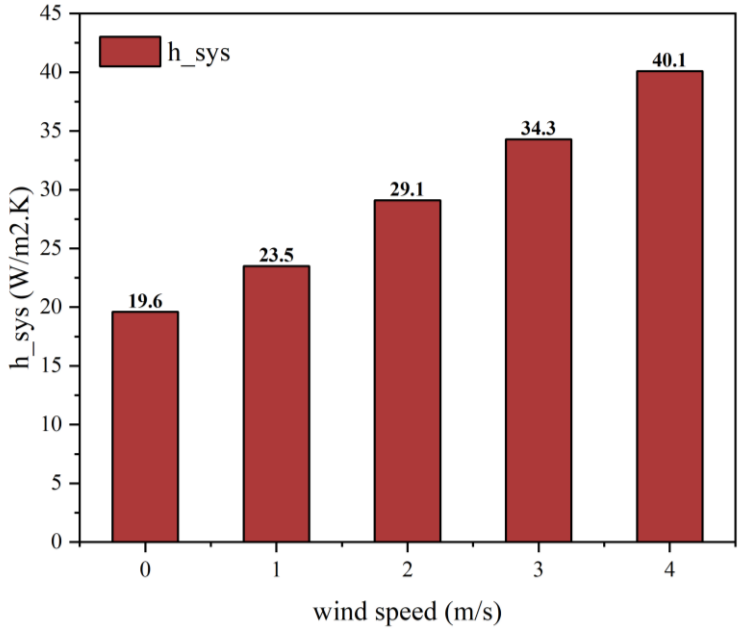

Figure 23: Effect of external wind speed on $\mathbf{h_{sys}}$.

Note. Increasing wind speed significantly increases h_{sys}, reflecting strong sensitivity to cavity ventilation. *By author*

4.3.3 Software simulation

Heat pumps usually require much higher mass flow rate (commonly > 700kg/h) and larger pipe diameters. These operating conditions may have large influence on $\mathbf{h_{sys}}$. To evaluate the façade's performance under realistic heat-pump operating conditions, numerical simulations were carried out using ANSYS Fluent software.

ANSYS is a widely used computational fluid dynamics (CFD) software in different engineering fields. It enables detailed simulation of steady-state conjugate heat transfer between solid layers, cavity airflow, and the circulating water.

1) Simulation setup

The simulation begins with the creation of a simplified A-Brick façade geometry **(Figure 24)**. A 0.5 m^2 façade section (1.0 m × 0.5 m) is modelled, consisting of a 20 mm ceramic layer, a 50 mm ventilated air cavity, and a 200 mm structural wall. The metal cassette is not included due to its negligible thickness (1 mm). A serpentine pipe with a 1 mm thickness and an inner diameter of 15 mm or 20 mm is positioned in the cavity adjacent to the ceramic surface, with 75 mm vertical spacing, consistent with the brick module.

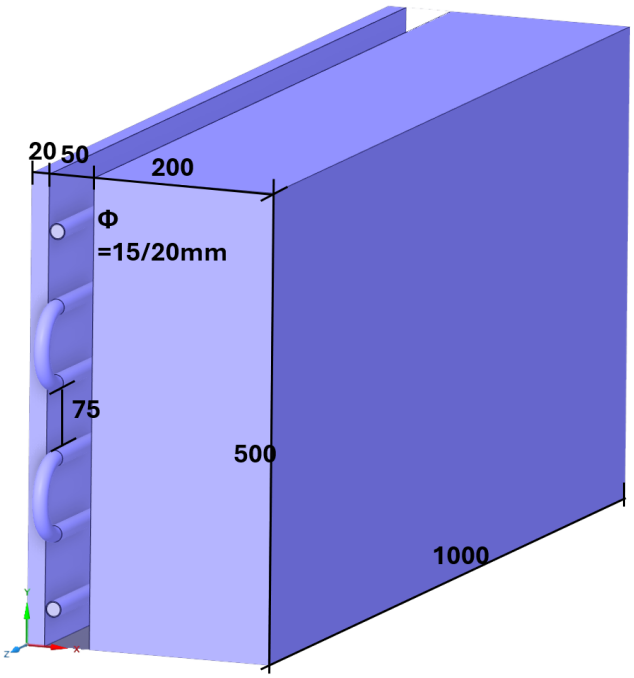

Figure 24: Simplified A-Brick ASTF geometry for ANSYS simulation. *By author*

A computational mesh is then generated, defining both solid and fluid regions along with inlet and outlet boundaries. Air flows from bottom to top while water flows from top to bottom. The mesh is densified around the water and pipe to ensure more accurate results.

The next step is to set boundary conditions. While outdoor temperature varies in different simulations, indoor temperature is constantly 20 degrees. Overall heat loss coefficient of outdoor surface is 12W/m^{2}K, considering slightly air convection and sky radiation. Overall heat loss coefficient of indoor surface is 7 W/m^2.K. Lateral surfaces are treated as adiabatic. Thermal conductivity of ceramic is 0.8 W/m·K, and thermal conductivity of structural wall is 0.2 W/m·K combined with thermal insulation.

Finally, steady-state solutions are computed. Average temperatures of each surface and visualized diagram are obtained to calculate h_{sys} and heat loss distribution.

2) Simulation results

Simulations are conducted in both heating and cooling modes with different outdoor temperatures, different water inlet temperature, and three levels of wind speed, and with identical configuration (ϕ15mm steel pipe) as well as fluid velocity (0.8m/s). Average outlet temperature is measured and $\mathbf{h_{sys}}$ is then calculated. The visualization shows in **Figure 25** and the results show in **Table 3.**

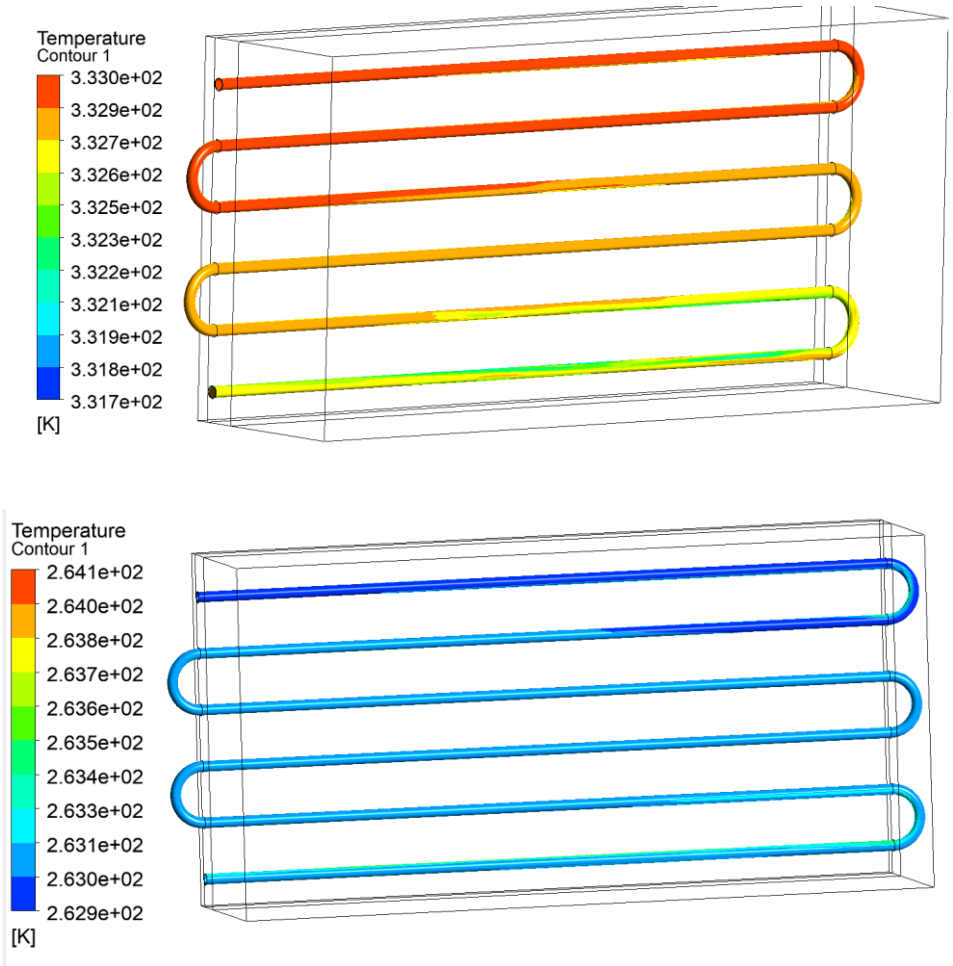

Figure 25: Visualization of steady-state water temperature in cooling and heating modes.

By author

Table 3

$h_{s\gamma s}$ under different outdoor temperatures, inlet water temperatures, and cavity wind speeds.

Outdoor Temperature	Inlet water temperature	h_{sys} under different cavity wind speed		
		0m/s	0.1m/s	0.5m/s
-10°C	-20 °C	15.2	19.9	23.0
	-16 °C	16.3	20.6	23.4
-5 °C	-20 °C	14.4	19.4	22.9
	-12 °C	15.5	20.2	23.3
0 °C	-20 °C	14.0	19.2	22.8
	-8 °C	14.7	19.9	23.2
5 °C	-20 °C	14.0	19.3	23.0
	-4 °C	14.5	19.7	23.2
10 °C	-20 °C	13.5	19.1	23.0
	0 °C	14.2	19.6	23.3
20 °C	40 °C	13.9	19.6	23.6
	30 °C	13.9	19.7	23.6
25 °C	45 °C	14.2	19.8	23.8
	35 °C	14.2	19.8	23.8
30 °C	50 °C	15.0	20.2	24.1
	40 °C	14.7	20.3	24.2

The simulation results indicate that $h_{s\gamma s}$ is primarily governed by cavity wind speed rather than by outdoor temperature or inlet water temperature. For a given wind speed, $\mathbf{h_{sys}}$ remains nearly constant across the full range of outdoor and inlet water temperatures. In contrast, increasing cavity wind speed from 0 m/s to 0.5 m/s consistently raises $h_{s\gamma s}$ from about 14–16 W/m^2K to approximately 23–24 W/m^2K. This confirms that air-side convection in the cavity is the dominant factor controlling the overall heat-transfer coefficient, while the influence of outdoor and inlet water temperatures on $h_{s\gamma s}$ is negligible within the investigated range.

It can obtain all surfaces' average temperature, which enable for calculating heat distribution. Heat distribution under different cavity air velocity show in **Figure 26**. The heat-distribution analysis further confirms that heat loss through the ceramic layer is also a dominant pathway, and its proportion increases as cavity wind speed decreases. Heat transferred toward the indoor side remains minimal, owing to the high thermal resistance of the insulated structural wall.

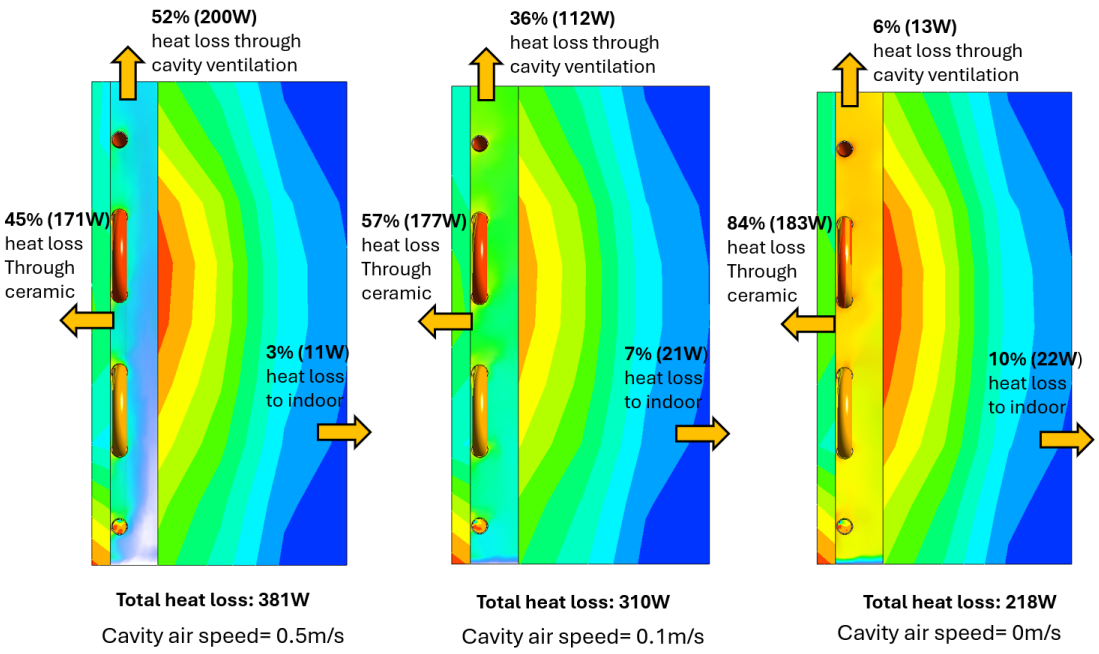

Figure 26: Heat distribution comparison under different cavity air velocity. *By author*

Variation of pipe diameter is conducted in identical wind speed (0.5m/s) and water speed (1.2m/s) but with different materials, the results are shown in **Figure 27**.

The results show that higher pipe conductivity and larger pipe diameter lead to higher $\mathbf{h_{sys}}$, although the magnitude of improvement is relatively moderate.

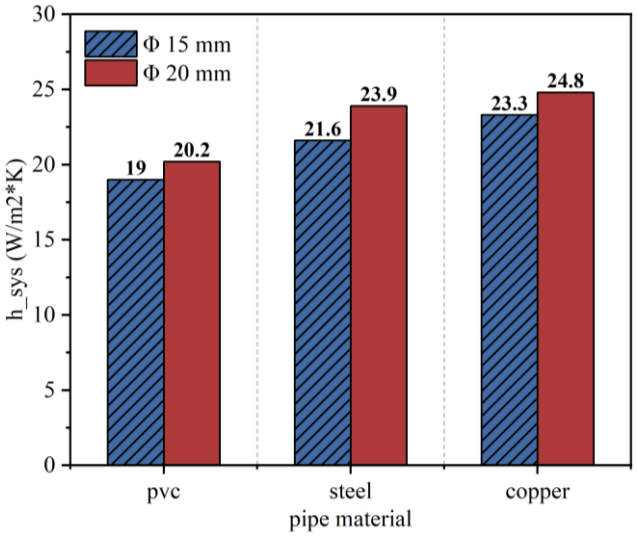

Figure 27: Effect of pipe diameter on $\mathbf{h_{sys}}$ comparing with different materials.

Note. Larger pipe diameter and higher thermal conductivity modestly increase $\mathbf{h_{sys}}$. *By author*

Variation of water flow speed and pipe material is conducted in identical wind speed (0.5m/s) and pipe diameter (ϕ15mm), the results are shown in **Figure 28.**

The results show that increasing the water flow speed from 0.8 m/s to 1.2 m/s results in a noticeable increase in the system heat-transfer coefficient. This improvement is observed consistently across all pipe materials. Higher flow velocity enhances internal convection and reduces the water-side thermal resistance, leading to higher overall heat-exchange performance. However, like material and diameter effects, the magnitude of improvement remains moderate.

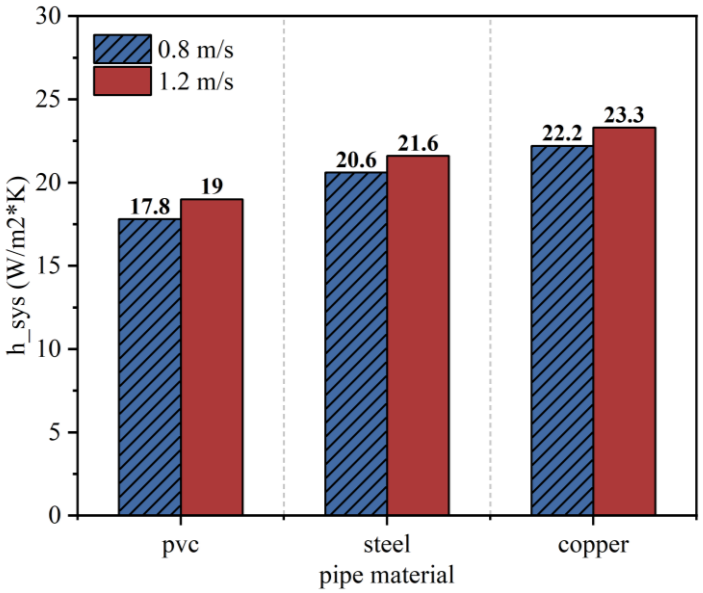

Figure 28: Effect of water velocity on $\mathbf{h_{sys}}$ comparing with different materials.

Note. Increasing water velocity from 0.8 m/s to 1.2 m/s enhances $\mathbf{h_{sys}}$ for all materials.

By author

5. Application of A-Brick ASTF on Energy Systems

This chapter evaluate thermal performance of A-Brick ASTF on system level with two representative applications: DHW preheating and heat-pump coupling. For each case, mathematical calculations are performed under realistic operating conditions to determine the façade area required to meet the thermal demand as well as energy output. In addition, TRNSYS simulations using annual weather data are carried out to estimate yearly DHW heat production and to evaluate the seasonal coefficient of performance (SCOP) of the heat-pump system.

5.1 DHW preheating calculation in solar collector mode

The working principle of DHW preheating has been explained in chapter 2. According to literature studies, DHW preheating typically operates seasonally. To determine which seasons can provide sufficient solar heat, Dutch weather data from South Holland was analysed in Grasshopper using the EPW weather file. The grasshopper tool enables calculating hourly solar radiation on southern, vertical façade by incorporating solar angle data. Assuming DHW preheating runs 6 hours per day from 10:00 to 16:00. Average solar radiation and dry bulb air temperature of each month (10:00-16:00) is calculated. Results are shown in **Table 4**. This table also includes average steady-state temperature that DHW preheating can finally reach, which can be calculated by **Equation (10)**: (Collector heat loss coefficient $\mathbf{h_L}$ =50W/m^{2}K considering outdoor convection and sky radiation)

$$T\infty = T_{\mathrm{a}} + \frac{G(\tau\alpha)}{h_{\mathrm{L}}} \tag{10}$$

Table 4

Average solar irradiance on southern, vertical façade, Average outdoor air temperatures and Average steady-state collector water temperature of each month from 10:00-16:00. Calculated by EPW weather file of South Holland province.

Months	G (W/m^2)	T_a (^{o}C)	$T\infty$ (^{o}C)
January	102	3.9	5.5
February	198	3.9	7
March	353	7.1	12.6
April	445	10.6	17.7
May	516	15.2	23.4
June	559	17.6	26.5
July	519	18.9	27.2
August	481	19.9	27.6
September	334	16.9	22.2
October	205	12.8	16.1
November	112	9.4	11.2
December	76	5.6	6.8

Table 4 shows that From March to September total solar radiation on South vertical façade is sufficient to provide heat. The average solar radiation in these months between 10:00 to 16:00 is 457 W/m^2. The average air temperature is 14°C. Assuming tap water temperature is equal to air temperature (normally tap water temperature is equal to 1m underground soil temperature (Blokker et al., 2013), which is close to the air temperature). The maximum steady-state temperature of collector water is 38°C.

For Dutch dwellings, the daily domestic hot water demand is typically assumed to be about 50 L/person per day (Blokker et al., 2009). Assume we are providing DHW for a 4-residence house, the total DHW need is 200L. The required daily heat to heat tap water to steady-state temperature by **Equation (5)**:

$$Q_{\text{load}} = mc\text{p}(T_{\max} - T0) = 200 \times 4184 \times (38 - 14) = 20.1 \times 10^6 J$$

Where:

$\boldsymbol{Q_{load}}$: Required heat for heating tap water to steady-state temperature (J)

$\boldsymbol{m}$: mass of DHW water (m^2)

$\boldsymbol{T_0}$: Initial tap water temperature, assumed equal to outdoor air temperature (°C)

The process of DHW preheating is same process as transient experiment in Chapter 4, with PVC-front configuration, 0.09m2 ASTF and 60kg/h mass flow rate, the transient progress of heating 1L water with 450W/m2 solar power shows in **Figure 29.**

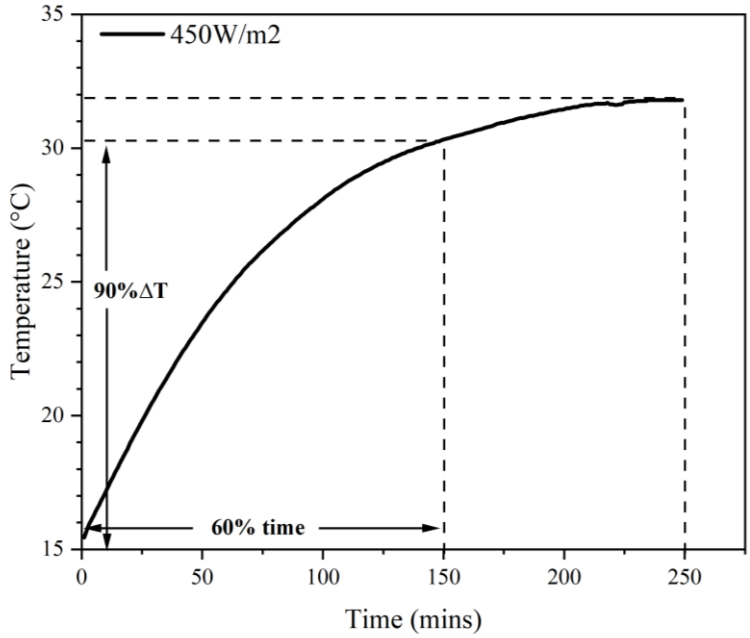

Figure 29: Transient heating profile of 1 L water under 450 W/m^2 irradiance.

Note. The figure illustrates to reach 90% of the temperature rise only requires 60% of time.

By author

Figure 25 shows that at 60% of the total time, the water has already risen 90% of total ΔT, so to keep system running in high efficiency, we let the system operation stop at the 90% of T∞-T0. The average efficiency in first 60% time can be calculated by **Equation (4)**:

$$\eta = \frac{Q_1}{G_1 A_1 t_1} = \frac{1 \times 4184 \times (30.2 - 15.5)}{450 \times 0.09 \times 9000} = 0.17$$

Where:

$\boldsymbol{\eta}$: Average solar collector efficiency

$\boldsymbol{Q_1}$: Total heat for 1L water to reach 90% of total ΔT (J)

$\boldsymbol{G_1}$: Solar heating power in the transient experiment (450W)

$\boldsymbol{A_1}$: ASTF surface area in transient experiment (0.09m^2)

$\boldsymbol{t_1}$: Total time for 1L water to reach 90% of total ΔT (s)

Then we can calculate the required ASTF surface area that heat tap water to 90% T∞-T0 during 6hrs:

$$A = \frac{0.9 Q_{\text{load}}}{\eta G t} = \frac{0.9 \times 20.1 \times 10^6}{0.17 \times 457 \times 21600} = 10.77m2$$

Where:

$\boldsymbol{A}$: Required ASTF surface for DHW preheating (m^2)

$\boldsymbol{\eta}$: Average solar collector efficiency measured by 450W transient experiment.

$\boldsymbol{G}$: Average solar irradiance from March to September between 10:00-16:00

$\boldsymbol{t}$: Total time for DHW preheating process (6 h)

Average ASTF energy output from March to September between 10:00-16:00 can be calculated as:

$$\dot{Q} = \eta G = 0.17 \times 457 = 77.7\ W/m2$$

Annual ASTF energy yield from March 1 to September 30 (214 days) by 3.14m^2 ASTF can be calculated as:

$$Q = 214 \times 0.9 \times Q_{\text{load}} = \frac{214 \times 0.9 \times 5.86 \times 10^6}{3.6 \times 10^6} = 313\ kWh$$

5.2 heat pump calculation in heat exchanger mode

The feasibility of connecting A-Brick ASTF with multifunctional air source heat pumps has already been examined in chapter 3. And thermal property of heat exchanger $\mathbf{h_{sys}}$=14-25 W/m^{2}K is measured in chapter 4. This section is going to calculate the required A-Brick ASTF surface area and heat exchange power rate.

Commonly heating load is the dominant factor in determining the required capacity of the heat pump. Therefore, heating load is calculated in this section. A well-insulated residential house with 150m2 living area is used in this case. The

required heating capacity is derived as the product of the building's heated floor area and the specified design heating load per unit area. This ensures the system is sized to meet the peak heat demand under design climatic conditions. According to Jakob et al. (2020), the design heating load of a well-insulated Dutch residential building is around 40W/m2. Design heating capacity of heat pump can be calculated as:

$$Q_{\text{heating}} = A \times q_{\text{design}} = 150 \times 40 = 6kW$$

Where:

$\boldsymbol{Q_{heating}}$: required heating capacity (kW)

$\boldsymbol{A}$: Living Area (m^2)

$\boldsymbol{q_{design}}$: design heating load per unit area (W/m^2)

A 6kW heat pump is selected to meet both the heating and cooling demands of the building. To determine the required A-Brick ASTF surface area, the first step is to calculate how much heat must be extracted from the outdoor air by A-Brick ASTF. In heating mode, the heat pump draws heat from the evaporator and delivers it to the indoor space through the condenser. The electrical input simply enables the transfer of heat from the colder outdoor environment to the warmer indoor environment. The heat balance of the heat pump system can be expressed by **Equation (11)**:

$$Q_{\text{evap}} + Q_{\text{elect}} = Q_{\text{cond}} + Q_{\text{loss}} \tag{11}$$

Where:

$\boldsymbol{Q_{evap}}$: Heat absorbed at the evaporator (kW)

$\boldsymbol{Q_{elect}}$: Electrical power input to the compressor (kW)

$\boldsymbol{Q_{cond}}$: Heat delivered at the condenser (kW)

$\boldsymbol{Q_{loss}}$: Heat losses that occur inside the heat pump system during operation (kW)

The Coefficient of Performance (COP) is a measure of how efficiently the heat pump delivers heating or cooling compared to the amount of electrical energy it consumes. By its definition, it can be calculated as:

$$COP = \frac{Q_{\text{cond}}}{Q_{\text{elect}}} \tag{12}$$

Combined **Equation (11)**, **(12)**, we can calculate the heat needed in evaporator side:

$$Q_{\text{evap}} = Q_{\text{cond}}\left(1 - \frac{1}{COP}\right) - Q_{\text{loss}} \tag{13}$$

In most practical heat-pump analyses, $\mathbf{Q_{loss}}$ can be neglected because the thermal losses from the refrigerant circuit and casing are very small compared to the useful heating output. Standard performance testing and manufacturer data typically show that these losses are within 1–3% of $\mathbf{Q_{loss}}$.

According to **Equation (13),** $\mathbf{Q_{cond}}$ is equal to the heating capacity of heat pump, system COP is still unknown. Heat pump COP can be calculated by **Equation (14)**.

$$COP = \eta_c \times COP_{\text{carnot, real}} \tag{14}$$

Where:

$\boldsymbol{\eta_c}$: Carnot efficiency of heat pump. for cheap systems $\boldsymbol{\eta_c}$ is smaller than 0.3 and for excellent systems $\boldsymbol{\eta_c}$ is around 0.6.

$\mathbf{COP_{Carnot,\ real}}$: Realistic Carnot COP.

The theoretical maximum COP is Carnot COP; it represents the upper efficiency limit that no real heat pump can exceed. However, A real heat pump does not heat or cool exactly at the supply temperature or the source temperature. the refrigerant evaporates at a temperature lower than the source temperature and the refrigerant condenses at a temperature higher than the water leaving the condenser. So, to calculate a realistic Carnot COP, we must use effective temperatures at evaporator and condenser. The realistic Carnot COP can be calculated by **Equation (15)**.

$$COP_{\text{carnot, real}} = \frac{T_{\text{cond}}}{T_{\text{cond}} - T_{\text{evap}}} = \frac{T_h + \Delta T}{T_h + \Delta T - (T_c - \Delta T)} \tag{15}$$

Where:

$\boldsymbol{T_h}$: hot side (load)temperature (K)

$\boldsymbol{T_c}$: cold side (source) temperature (K)

$\boldsymbol{T_{cond}}$: condensing temperature (K)

$\boldsymbol{T_{evap}}$: evaporating temperature (K)

$\Delta\boldsymbol{T}$: Temperature difference between source (water-glycol) and refrigerants in evaporator (K)

To size the ASTF surface area, the system is evaluated under the most demanding winter conditions. According to the Dutch standard ISSO 51, the design outdoor temperature is the coldest-day temperature, taken as –10 °C. For a 40% water–glycol mixture, the minimum operating temperature is approximately –20 °C. The temperature lift across the heat pump evaporator typically ranges from 3–5 °C. To determine the minimum required ASTF area, a smaller temperature difference is selected—$\mathbf{\Delta T}$ = 3 °C—because a lower evaporator temperature results in a larger log-mean temperature difference $\mathbf{\Delta T_{lm}}$ between the working fluid and the outdoor air, thereby increasing the required heat extraction surface. The schematic system configuration is shown in the **Figure 30**.

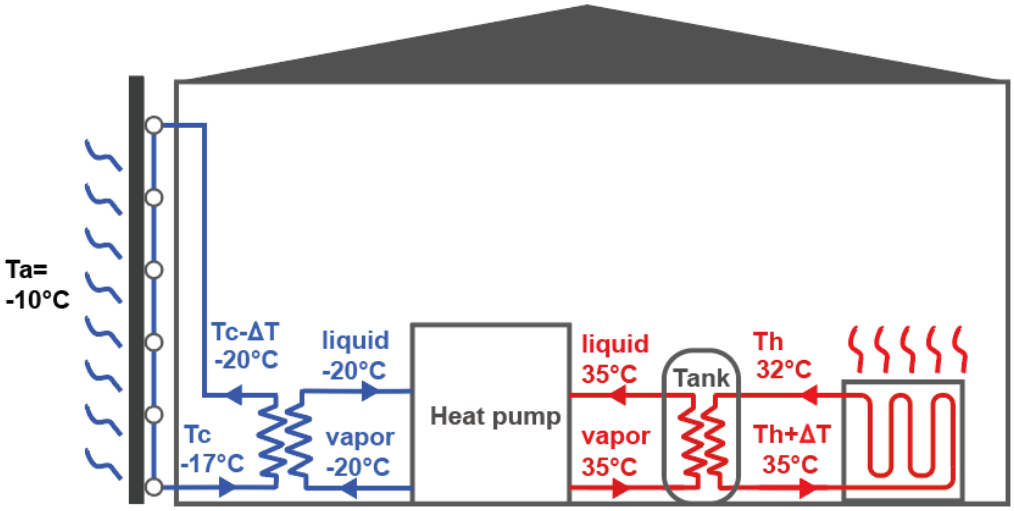

Figure 30: Schematic of Heat Pump Operation and ASTF Heat Extraction.

Note. Temperature profile of the heat pump and ASTF system at −10 °C design conditions. *By author*

Assuming Carnot efficiency $\boldsymbol{\eta_c}$ =0.5. For given conditions, system COP can be calculated by **Equation (14)** and **(15)**:

$$COP = 0.5 \times \frac{273 + 35}{273 + 35 - (273 - 20)} = 2.8$$

Then required heat extraction by ASTF can be calculated by **Equation (13)**

$$Q_{\text{evap}} = 6\left(1 - \frac{1}{2.8}\right) = 3.85kW$$

Using back-mounted steel pipes and assuming an average air-cavity wind speed of 0.1 m/s, the system heat-transfer coefficient $\mathbf{h_{sys}}$ reaches approximately 20 W/m^2·K. The log-mean temperature difference $\mathbf{\Delta T_{lm}}$ is then determined using **Equation (9)**, then the required surface area can be calculated using **Equation (8)**:

$$\Delta T_{\text{lm}} = \frac{-20 - (-17)}{\ln\left(\frac{-20 - (-10)}{-17 - (-10)}\right)} = 8.4°C$$

$$A = \frac{Q_{\text{evap}}}{h_{\text{sys}}\Delta T_{\text{lm}}} = \frac{3850}{20 \times 8.4} = 22.8m2$$

The required mass flow rate and the corresponding number of parallel pipe circuits must also be determined to ensure adequate thermal delivery. The necessary mass flow rate for the ASTF system can be calculated by **Equation (5)**:

$$\dot{m} = \frac{Q_{\text{evap}}}{c_{\text{p}}(T_{\text{in}} - T_{\text{out}})} = \frac{3850}{4184 \times 3} = 0.31 kg/s$$

With 40% Water-glycol mixtures, fluid velocity between 0.8m/s to 1.2m/s is recommended. Because it provides a good balance between heat-transfer performance and hydraulic efficiency. At this velocity, the flow is fully turbulent, ensuring a high internal heat-transfer coefficient, while the pressure drop and pump power remain at reasonable levels. It also avoids the noise, vibration, and erosion risks that occur at higher velocities (>1.2 m/s). For different diameter's pipe, the mass flow rate at 0.8/s velocity shows in **Table 5.**

Table 5

Mass flow rate at 0.8 m/s for different pipe diameters

Pipe diameter	Mass flow rate (kg/s)
10 mm	0.06
12 mm	0.09
15 mm	0.14
20 mm	0.25
22 mm	0.31
25 mm	0.39

According to the **Table 5**, 4*Φ12 mm that can be arranged in parallel to collectively meet the flow demand. These parallel sub-pipes then merge into a Φ22mm main pipe, as illustrated in **Figure 31.**

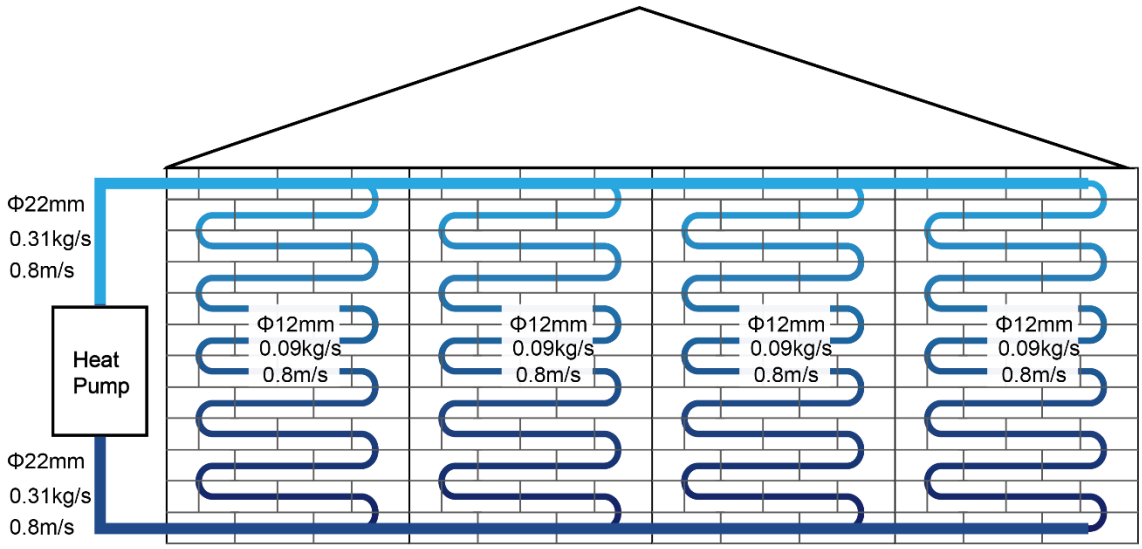

Figure 31: Parallel Φ12 mm Sub-Pipe Arrangement and Integration into a Φ22 mm Main Pipe for Heat Pump Circulation. *By author*

5.3 TRNSYS simulation

To evaluate the seasonal performance of coupling the A-Brick ASTF with a water-source heat pump, a detailed system model was developed in TRNSYS. This chapter simulates the heating operation for a single winter day (January 1st) as well as an extended two-month period from January 1st to March 1st. The simulations provide temperature profiles across all system components and quantify the heat pump's Seasonal Coefficient of Performance (SCOP) under Dutch winter climatic conditions.

Component explanation and setup

Type 15-2: **Weather file** of South Holland province.

Type 559: **Flat-plate heat exchanger.** It has a 25m^2 surface area. And the fixed heat loss coefficient $\mathbf{h_{sys}}$ is 20W/m^{2}K**.** $\mathbf{h_{sys}}$ will be increased by combining with Ambient temperature, Sky radiation and wind velocity from weather file.

Type534: **Heat-exchanger water tank.** Heat is exchanged in this component between ASTF's water glycol and heat pump's refrigerant.

Type 114: **Water pump**. Mass flow rate is 1100kg/h

Type 927: **Water to water heat-pump.** Rated heating capacity is 8kW. Rated electricity power is 1.5kW

Type 158: **Water storage tank.** The heat produced by heat pump is storage here.

Type 2b: **Operation signal control component.** When the water in storage tank reaches the upper setting point. The heat pump stop working. When the temperature is down to the lower setting point. The heat pump runs again.

Type 682: **Heating loads.** Heating loads is constantly 6kW.

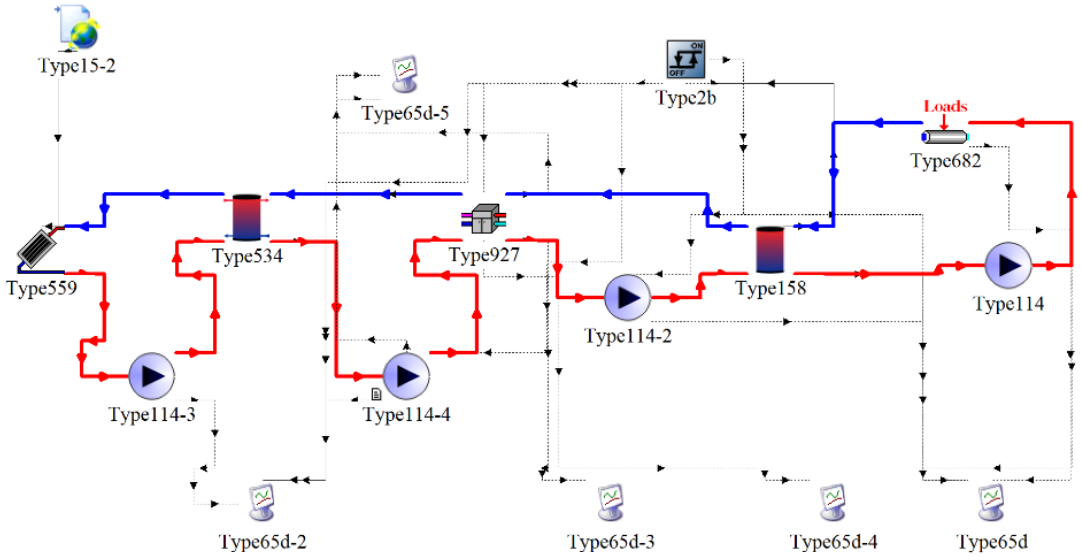

Figure 32: TRNSYS system configuration. *By author*

The simulation results indicate that the water–glycol entering the ASTF heat exchanger at approximately **3 °C**, while the outlet temperature increases to around **8 °C**, yielding an average temperature lift of **5 °C** across the façade panel. Throughout the day, the outlet temperature closely follows the ambient air temperature, with only a small offset, demonstrating strong thermal coupling between the ASTF water loop and the outdoor environment.

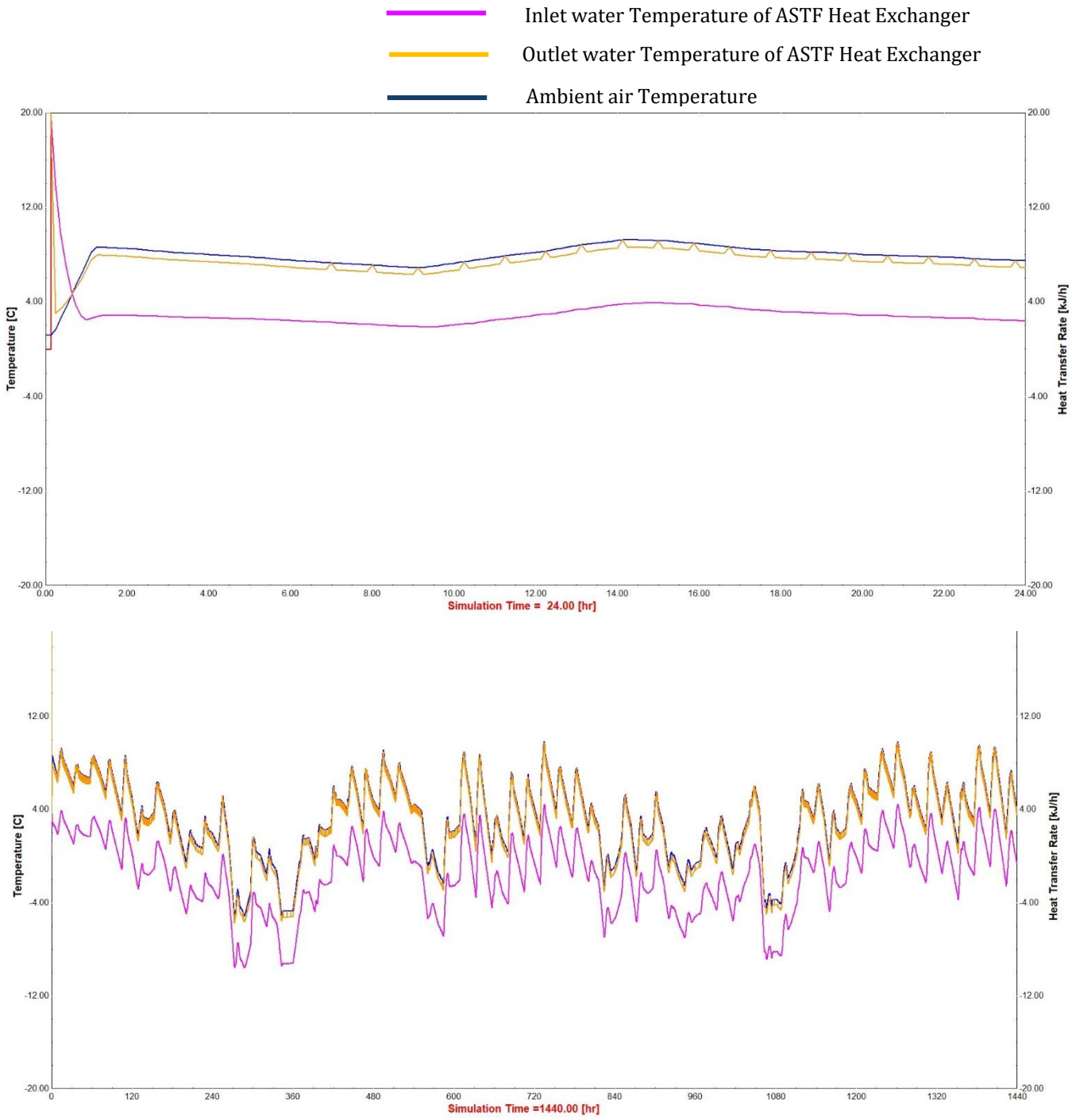

Figure 33: Results of Temperature at ASTF inlet and outlet.

Note. The first figure shows results on January 1st. The second figure shows results between January 1st and March 1st. *By author*

The simulation results indicate that the evaporating temperature as same as water-glycol source temperature, and condensing temperature is fluctuated around 35**°C**, controlled by the temperature monitor. Temperature difference at both condenser and evaporator is 5 **°C.** The results indicating reliable operation and effective thermal matching with the ASTF water–glycol source.

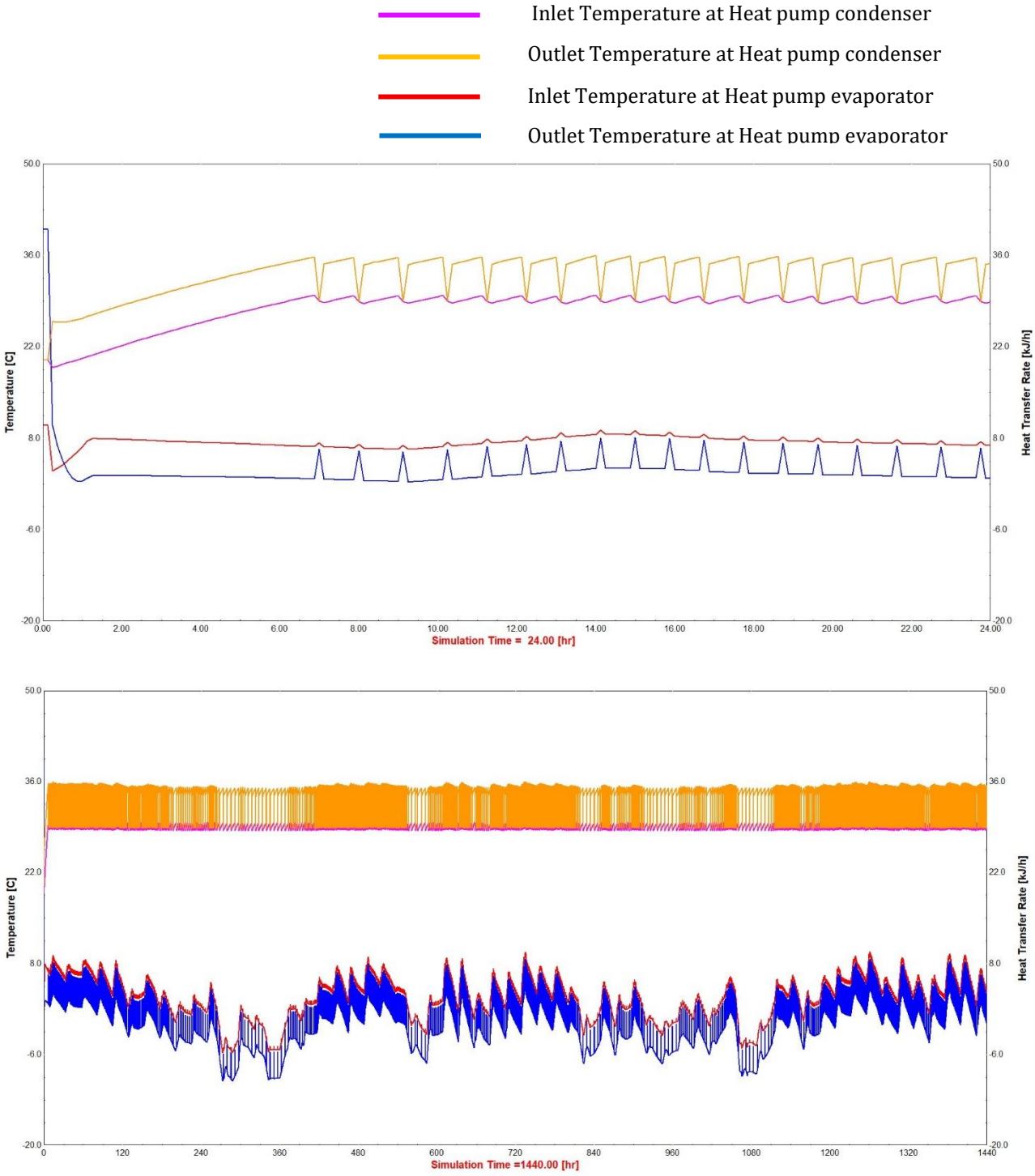

Figure 34: Results of Temperature at Heat pump's evaporator and condenser

Note. The first figure shows results on January 1st. The second figure shows results between January 1st and March 1st. *By author*

The two-month simulation between January 1st and March 1st yields a SCOP of **4.2**, showing that the A-Brick ASTF provides a steady low-grade heat source that improves winter performance of the heat pump (**Figure 35**). The façade keeps the water–glycol source temperature consistently in the **3–5 °C** range, avoiding exposure to the coldest outdoor temperatures. As a result, the heat pump operates with more stable evaporating conditions, reduced cycling, and a higher overall efficiency. These results confirm that the ASTF effectively enhances the heat pump's seasonal performance and serves as a reliable supplementary heat source during cold periods.

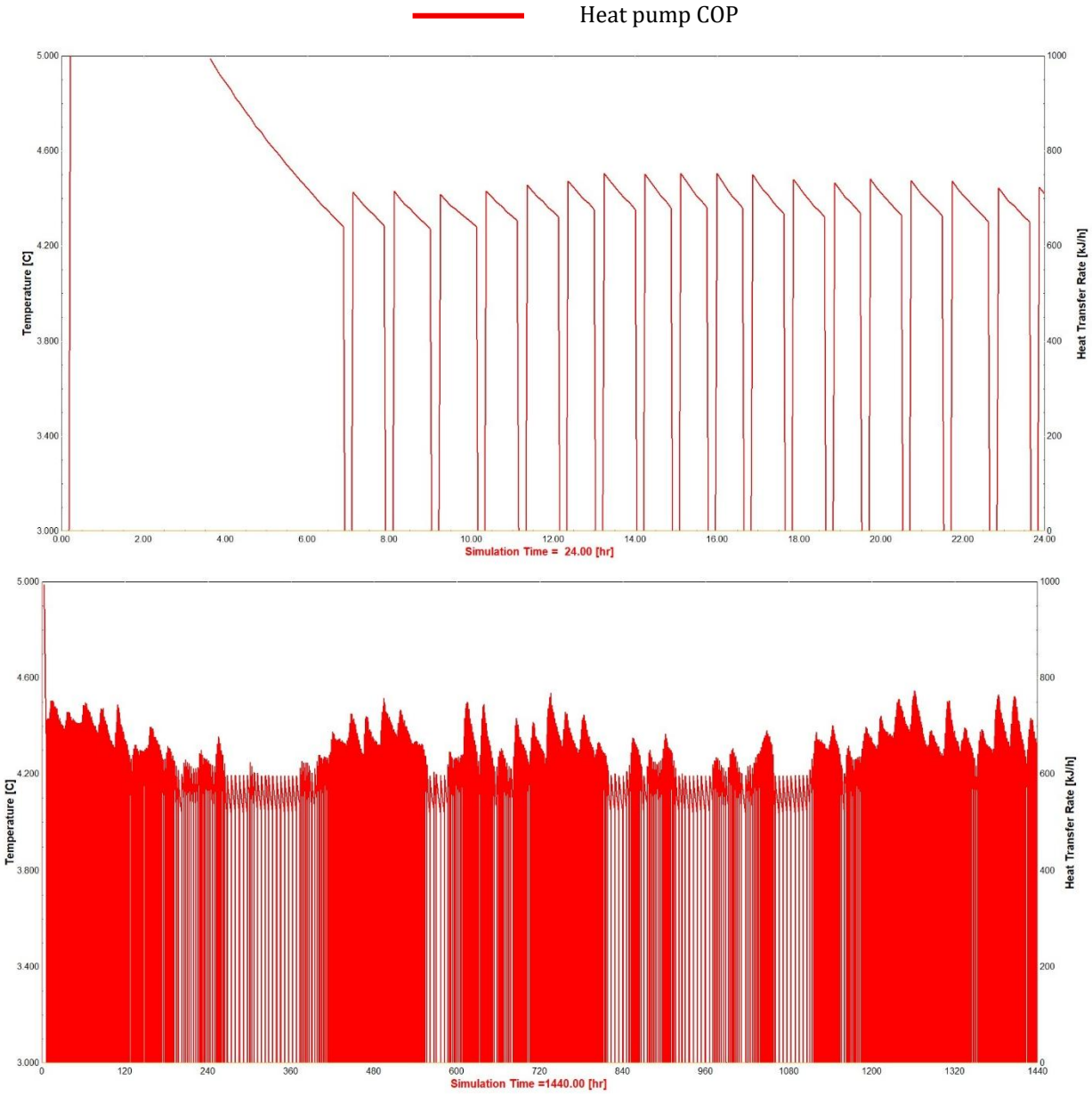

Figure 35: Results of Temperature at Heat pump's COP

Note. The first figure shows results on January 1st. The second figure shows results between January 1st and March 1st. *By author*

5.4 Design manual

The A-Brick ASTF Design Manual (**Figure 36**) provides practical sizing guidelines for integrating ASTF into residential buildings, covering three major application scenarios: heat pump, air-conditioning (cooling mode only) and DHW preheating. These tables serve as a quick reference for engineers, designers, and installers to estimate system scale, plan hydraulic layouts, and evaluate annual energy gains when applying ASTF in real building projects.

Heat pump (Heating & Cooling)

Heating capacity	*ASTF area*	*Flow rate*	*Pipe configuration*		
4 kW	15.2 m^2	734 L/h	3×Φ12	2×Φ15	1×Φ20
6 kW	22.8 m^2	1101 L/h	4×Φ12	3×Φ15	2×Φ20
8 kW	30.5 m^2	1468 L/h	5×Φ12	3×Φ15	2×Φ20
10 kW	38.1 m^2	1836 L/h	6×Φ12	4×Φ15	2×Φ20
12 kW	45.7 m^2	2202 L/h	7×Φ12	5×Φ15	3×Φ20
15 kW	57.1 m^2	2753 L/h	9×Φ12	6×Φ15	3×Φ20

Heat pump efficiency ηc=0.5 ASTF h _ sys=20W/m2K

Air conditioner (Cooling mode only)

Cooling capacity	*ASTF area*	*Flow rate*	*Pipe configuration*		
2 kW	8.9 m^2	765 L/h	3×Φ12	2×Φ15	1×Φ20
3.5 kW	15.6 m^2	1339 L/h	5×Φ12	3×Φ15	2×Φ20
5 kW	22.2 m^2	1913 L/h	6×Φ12	4×Φ15	2×Φ20
8 kW	35.6 m^2	3060 L/h	10×Φ12	6×Φ15	4×Φ20
10 kW	44.4 m^2	3823 L/h	12×Φ12	8×Φ15	5×Φ20

Air conditioner COP=4 ASTF h _ sys=20W/m2K

DHW preheating (April – September 10:00-16:00)

Residence people	*Water volume*	*ASTF area*	*ASTF power*	*Annual gain*
1	50 L	0.79 m^2	71 W	77 kWh
2	100 L	1.57 m^2	141 W	154 kWh
3	150 L	2.36 m^2	211 W	231 kWh
4	200 L	3.14 m^2	282 W	308 kWh
6	300 L	4.71 m^2	423 W	462 kWh
10	500 L	31.4 m^2	705 W	770 kWh

Figure 36: ASTF design manual. *By author*

6. Discussion

Discussion with ASTF solar collector

Steady-state prototype experiments show that as a solar collector, the A-Brick ASTF exhibits relatively low collector efficiency between **15–30%**. Which is much lower than conventional plat-plate collector which collector efficiency is normally between **50%-70%**. This reduced performance can be attributed to two primary factors. First, the system experiences substantial heat loss ($\mathbf{h_L=41}$), because the absorber plate is directly exposed to outdoor environment, causing a high convection and radiation lost. Second, the heat removal factor $\mathbf{F_R}$ is **0.25-0.35**, which is quite low, reflecting limited thermal coupling between the ceramic surface and the working fluid. The results are expected, as the absence of a glazing cover allows greater heat loss, and the air gap between the water pipes and the ceramic cladding further reduces the overall thermal coupling.

The transient experiments illustrate the influence of different variables on the system's performance. The results shows that front-mounted pipes achieve higher collector efficiency than back-mounted pipes, but the limited pipe diameter (<10 mm) make front-mounted pipes more suitable for small systems requiring low mass flow rates such as DHW preheating.

For **DHW preheating**, the analysis shows that south-facing ceramic façades receive sufficient solar irradiance from March to September, with an average façade-incident radiation of $\mathbf{457\ W/m^2}$ during daytime operation. Based on the steady-state experiments in Chapter 4, the system achieved an average efficiency of 17% under 450 W/m^2 irradiance when heating 1 L of water to 90% of its total temperature rise. This experimentally derived efficiency was then used to back-calculate the required façade area for seasonal DHW preheating. The results indicate that a $\mathbf{10.77\ m^2}$ A-Brick ASTF surface is capable of heating **200 L** of tap water to 90% of the steady-state temperature rise within 6 hours, delivering approximately **313 kWh** of useful thermal energy during the heating season. These findings suggest that A-Brick ASTF can provide a meaningful contribution to residential DHW production during months with sufficient solar availability.

Discussion with ASTF heat exchanger

When operating as a heat exchanger, the A-Brick system achieves an overall heat-transfer coefficient $\mathbf{h_{sys}}$ of approximately $\mathbf{14–25\ W/m^2K}$, with performance primarily governed by air-side convection. This range is moderate compared with typical shell-and-tube heat exchangers ($\mathbf{40–50\ W/m^2K}$) or outdoor fan-coil units ($\mathbf{80–120\ W/m^2K}$). The lower values are mainly due to the limited cavity airflow (0–0.5 m/s), which restricts convective heat transfer, and the minimal direct contact between the water pipes and the metal cassette, which reduces conductive heat transfer through the façade assembly. The results also show that for a given wind speed, $\mathbf{h_{sys}}$ remains nearly constant across the full range of outdoor and inlet

water temperatures. Heat-distribution analysis also shows that large portion of the released heat ultimately passes through the ceramic layer to the outdoor environment, highlighting the importance of outdoor wind convection and sky radiation. Increasing fluid velocity, pipe material conductivity, and pipe diameter all improve $\mathbf{h_{sys}}$, but their influence is moderate compared with the strong effect of air-side convection. Because of the moderate effect of pipe material conductivity, steel is recommended as the pipe material, as it offers substantially lower cost with only a minor reduction in thermal performance compared to copper.

Although the thermal performance heat exchanger is lower than conventional products, the façade's large available surface area compensates for its lower thermal property. Thus, ASTF still have great potential to be applied on heat pump systems.

For heat-pump operation, COP was estimated under extreme winter design conditions (−10 °C). By combining the evaporator heat demand with the measured heat-exchange coefficient hsys, a $\mathbf{22.8\ m^2}$ façade area was found sufficient to operate a **6kW** heat pump for a 150 m^2 well-insulated dwelling. TRNSYS simulation further suggests a seasonal COP of **4.2**, indicating promising system-level performance. The pipe-network strategy using parallel sub-pipes also shows that ASTF can meet the high flow-rate requirements of practical heat-pump systems, providing a pathway for scaling to larger buildings.

Limitations

Several limitations should be acknowledged when interpreting the system-level findings. First, the Chapter 4 experiments were conducted indoors under controlled conditions, without outdoor wind convection or sky-radiation heat loss. This likely led to lower $\mathbf{h_{sys}}$ or $\mathbf{h_L}$. Second, In laboratory prototype experiment, the water pipe extends out of the ceramic surface about 1/4 total length, that exposed segments may increase the measured $\mathbf{h_{sys}}$. Third, the spectrum of halogen lamps is larger than solar radiation, which leads to a small solar power meter reading number. The solar irradiance used in the experiment was therefore calculated by converting the solar power meter's reading into a full-spectrum value, the results may not be in high precision. Fourth, ANSYS simulation uses a simplified geometric model in which the ceramic cladding was treated as a continuous closed solid, while the actual A-Brick façade contains air gaps between each other that allow air movement. This simplification affects the predicted convection behaviour and heat-transfer performance.

In addition to the experimental limitations, several simplifications were made in the DHW and heat-pump calculations. The DHW estimation based on monthly average irradiance and air temperature, which cause insufficient or oversufficient in the real weather. Tap-water temperature was approximated using outdoor air temperature, whereas in reality tap water is influenced by shallow soil conditions and varies less than air temperature. The heat-pump sizing assumed an minimum

glycol temperature (−20 °C) and stable flow velocity, conditions that may not be fully achievable in practice and could reduce the effective ΔTlm and increase the required façade area in real operation.

7. Conclusion

Through a combination of literature review, laboratory prototype testing, numerical simulations, and system-level calculations, this research reaches a clear answer to the research question:

"In what ways can Aberson's A-Brick façade be developed into an effective Active Solar Thermal Façade (ASTF), and how effective is the system's thermal performance when integrated with different building energy systems?"

The findings confirm that the A-Brick façade can operate successfully in both solar-collector and heat-exchanger modes. Although the system exhibits lower thermal performance than conventional glazed collectors or fan-coil evaporators, its large available surface area compensates for the reduced efficiency, enabling meaningful energy contributions. Experiments and simulations consistently show that the system delivers stable thermal behavior and that its performance is sufficient to support low-temperature applications such as DHW preheating as well as heat-pump evaporator operation when appropriately sized.

System-level analyses further demonstrate practical feasibility. For a typical dwelling, a modest south-facing façade can supply a significant share of seasonal DHW demand, while a larger façade area can provide the required evaporator load for heat pump even under winter design conditions. The TRNSYS results also indicate that coupling the façade with a multifunctional heat pump can achieve high seasonal efficiency, underscoring the potential of façade-integrated renewable systems in residential buildings.

Overall, this study shows that the A-Brick façade can be transformed into a functional ASTF with practical applications in low-temperature energy systems. Its modular construction, aesthetic integration, and multifunctionality offer advantages over conventional external installations, particularly for dense urban environments. However, the present results remain preliminary. Further work is needed to validate the façade under real outdoor conditions, quantify full-scale DHW and heat-pump performance, and address practical engineering considerations such as long-term durability, leakage risks, and cost optimization. Nonetheless, the research establishes a solid technical foundation for advancing A-Brick ASTF development toward market-ready applications.

References

Amin, Z. Mohd., & Hawlader, M. N. A. (2013). A review on solar assisted heat pump systems in Singapore. *Renewable and Sustainable Energy Reviews*, *26*, 286–293. https://doi.org/10.1016/j.rser.2013.05.032

Buker, M. S., & Riffat, S. B. (2016). Solar assisted heat pump systems for low temperature water heating applications: A systematic review. *Renewable and Sustainable Energy Reviews*, *55*, 399–413. https://doi.org/10.1016/j.rser.2015.10.157

Blokker, E. J. M., Vreeburg, J. H. G., & Van Dijk, J. C. (2009). Simulating Residential Water Demand with a Stochastic End-Use Model. Journal Of Water Resources Planning And Management, 136(1), 19–26. https://doi.org/10.1061/(asce)wr.1943-5452.0000002

Blokker, E. J. M., & Pieterse-Quirijns, E. J. (2013). Modeling temperature in the drinking water distribution system. Journal - American Water Works Association, 105(1), E19–E28. https://doi.org/10.5942/jawwa.2013.105.0011

Chow, T. T., Bai, Y., Fong, K. F., & Lin, Z. (2012). Analysis of a solar assisted heat pump system for indoor swimming pool water and space heating. *Applied Energy*, *100*, 309–317. https://doi.org/10.1016/j.apenergy.2012.05.058

Dannemand, M. ;, Furbo, S. ;, Andersen, C., Amtrup, ;, Heller, A. ;, & Madsen, H. (2025). General rights Heating of indoor swimming pools by solar thermal collectors in summerhouses in Denmark. In *Downloaded from orbit.dtu.dk on*. www.byg.dtu.dk

Duffie, J. A. ., & Beckman, W. A. . (2013). *Solar engineering of thermal processes*. Wiley.

Elguezabal, P., Lopez, A., Blanco, J. M., & Chica, J. A. (2020). Assessment on the Efficiency of an Active Solar Thermal Facade: Study of the Effect of Dynamic Parameters and Experimental Analysis When Coupled/Uncoupled to a Heat Pump. *Energies*, *13*(3), 597. https://doi.org/10.3390/en13030597

Jakob, M., Reiter, U., Krishnan, S., Louwen, A., & Junginger, M. (2020). Chapter 11 – Heating and cooling in the built environment. In M. Junginger & A. Louwen (Eds.), Technological Learning in the Transition to a Low-Carbon Energy System: Conceptual Issues, Empirical Findings, and Use in Energy Modeling (pp. 189–219). Academic Press. https://doi.org/10.1016/B978-0-12-818762-3.00011-X

Kamps, B. L. M. (2023). *A review of domestic hot water production in the Netherlands*.

Kuang, Y. H., & Wang, R. Z. (2006). Performance of a multi-functional direct-expansion solar assisted heat pump system. *Solar Energy*, *80*(7), 795–803. https://doi.org/10.1016/j.solener.2005.06.003

Li, X., Qiu, H., Wang, Z., Li, J., Yuan, G., Guo, X., & Jin, L. (2023). Numerical Investigation of a Solar-Heating System with Solar-Tower Receiver and Seasonal Storage in Northern China: Dynamic Performance Assessment and Operation Strategy Analysis. *Energies*, *16*(14), 5505. https://doi.org/10.3390/en16145505

Nouri, G., Noorollahi, Y., & Yousefi, H. (2019a). Designing and optimization of solar assisted ground source heat pump system to supply heating, cooling and hot water demands. *Geothermics*, *82*, 212–231. https://doi.org/10.1016/j.geothermics.2019.06.011

Nouri, G., Noorollahi, Y., & Yousefi, H. (2019b). Solar assisted ground source heat pump systems – A review. *Applied Thermal Engineering*, *163*, 114351. https://doi.org/10.1016/j.applthermaleng.2019.114351

Nuntaphan, A., Chansena, C., & Kiatsiriroat, T. (2009). Performance analysis of solar water heater combined with heat pump using refrigerant mixture. *Applied Energy*, *86*(5), 748–756. https://doi.org/10.1016/j.apenergy.2008.05.014

O'Hegarty, R., Kinnane, O., & McCormack, S. (2015). A Case for Façade Located Solar Thermal Collectors. *Energy Procedia*, *70*, 103–110. https://doi.org/10.1016/j.egypro.2015.02.104

Trillat-Berdal, V., Souyri, B., & Fraisse, G. (2006). Experimental study of a ground-coupled heat pump combined with thermal solar collectors. *Energy and Buildings*, *38*(12), 1477–1484. https://doi.org/10.1016/j.enbuild.2006.04.005

Wang, Z., Guo, P., Zhang, H., Yang, W., & Mei, S. (2017). Comprehensive review on the development of SAHP for domestic hot water. *Renewable and Sustainable Energy Reviews*, *72*, 871–881. https://doi.org/10.1016/j.rser.2017.01.127

Zhang, X., Shen, J., Lu, Y., He, W., Xu, P., Zhao, X., Qiu, Z., Zhu, Z., Zhou, J., & Dong, X. (2015). Active Solar Thermal Facades (ASTFs): From concept, application to research questions. *Renewable and Sustainable Energy Reviews*, *50*, 32–63. https://doi.org/10.1016/j.rser.2015.04.108

Appendix: Assembly concept

A-Brick system is a modular system; the assembly sequence of A-Brick system is easy and high efficiency. The wooden keels are first fixed on the building structure wall. Then metal cassettes which have hooks and barbs on them are fixed on the wooden keels by bolts. The ceramic strip is lowered onto the hooks via its groove and then pressed at the top until it locks into the barbs.

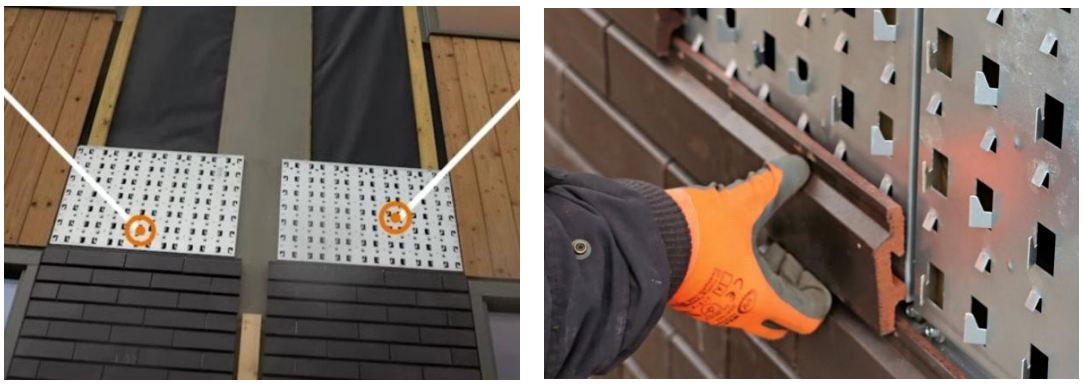

Figure 37: A-Brick façade installation. Source: Aberson's website, https://www.aberson.nl/producten/gevelsystemen/a-brick/

6.1 Solar collector assembly sequence

For the front-mounted DHW-preheating configuration, the assembly process is straight forward. The water pipe is positioned inside the 10 mm vertical gap between two ceramic claddings (**Figure 38**).
The installation proceeds as follows:

1. Install the first ceramic strip onto the metal cassette as usual.
2. Lay the flexible pipe on the 10 mm top ledge of the installed ceramic strip.
3. Install the next ceramic strip, which clamps the pipe naturally within the inter-cladding gap.
4. Because the pipe is flexible, it bends around the side of the ceramic strip and rests on top of the next ceramic piece, allowing continuous routing along the façade.

Figure 38: Solar collector water pipe installation. *By author*

6.2 Heat exchanger assembly sequence

In heat exchanger mode, serpentine water pipe is placed at the back of the metal cassette (**Figure 39**). Like ceramic claddings, the serpentine pipe is placed on a new row of barbs. To enable easy installation, compression fittings are used to connect two serpentine pipes. It will firstly slide the compression nut and ring onto each pipe, insert the pipe ends into the fitting body until fully seated, then tighten the nuts by hand. To provide spaces for connecting compression fittings, 30mm*70mm openings are created on metal cassettes, located on the diagonal of the metal cassette.

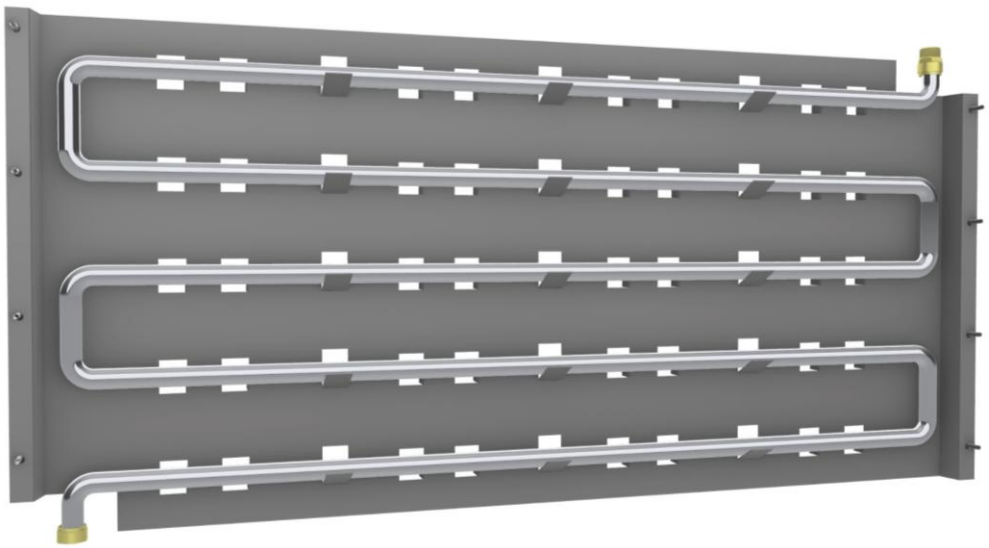

Figure 39: The way of attaching serpentine pipe on metal cassette. *By author*

The assembling sequence is (**Figure 40**):

1. Fix first metal cassette-serpentine pipe unit on wooden keel.
2. Put next unit in position and insert the end of serpentine pipe in the compression fitting
3. Screw bolts to fix the unit on the wooden keel
4. Tightening the compression fitting
5. Repeat the procedure until all units are fixed on the wooden keel
6. Click on all the ceramic strips

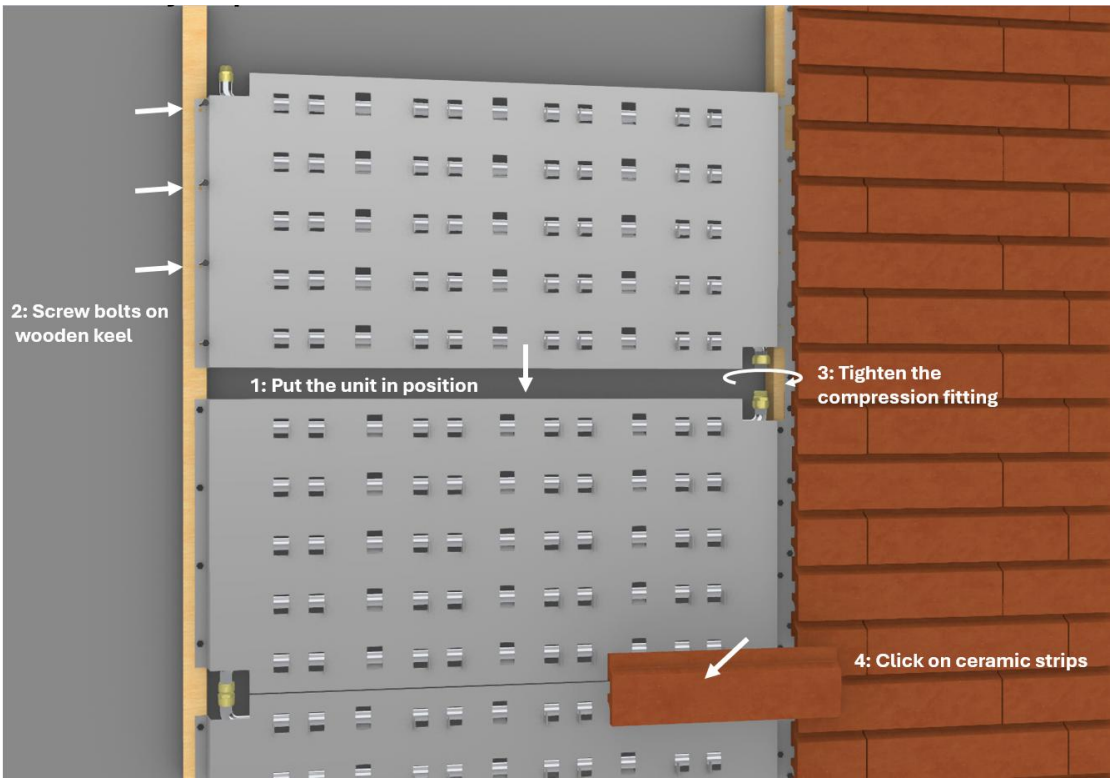

Figure 40: Heat exchanger ASTF assembly sequence. *By author*

A Rhino model is created to show how to apply the assembly to real cases. A ϕ22 mm main supply pipe is installed at the top of the façade, exiting from the indoor heat pump unit and passing through the exterior wall to run horizontally along the upper edge of the façade. The main pipe distributes flow to the vertical branch pipes through T-junctions equipped with small flow-control valves.
Each branch pipe then descends vertically along the façade. In the ideal configuration, every branch should run continuously downward until it reaches the main return pipe at the bottom, avoiding any upward bends. Eliminating

upward segments ensures that gravity assists the downward flow and prevents flow maldistribution caused by water being forced to climb against gravity.
However, when branch pipes must bypass façade elements—such as windows, doors, or structural openings—a short horizontal bypass unit becomes unavoidable. The horizontal units allow the pipe to detour around the obstacle before continuing its vertical descent toward the return pipe.
A circulation pump is installed at the end of the return line, enabling the return water to be driven vertically upward back into the heat pump unit.

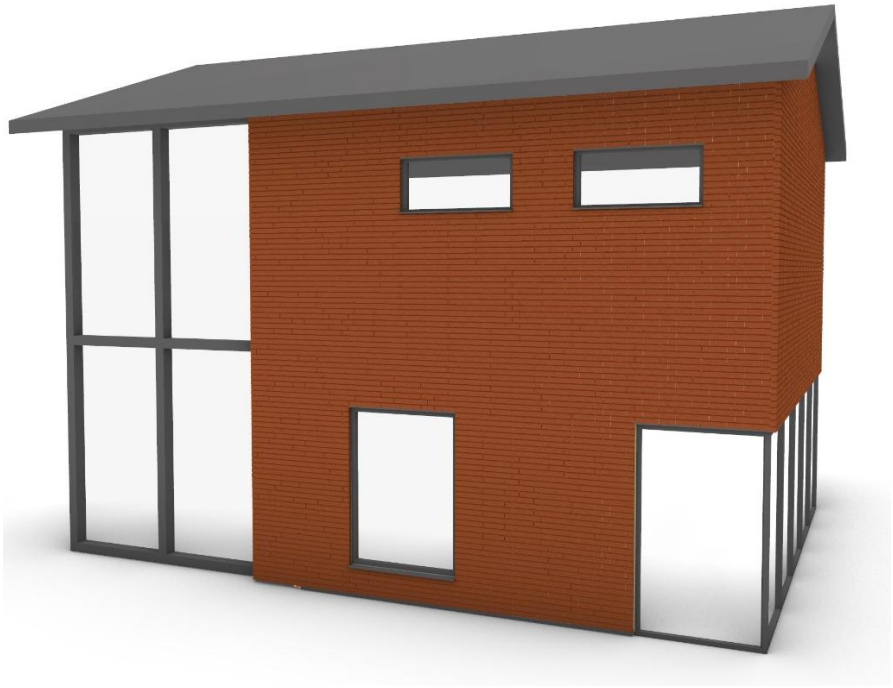

Figure 41 Different layers of A-Brick ASTF when applying on a building. B*y author*

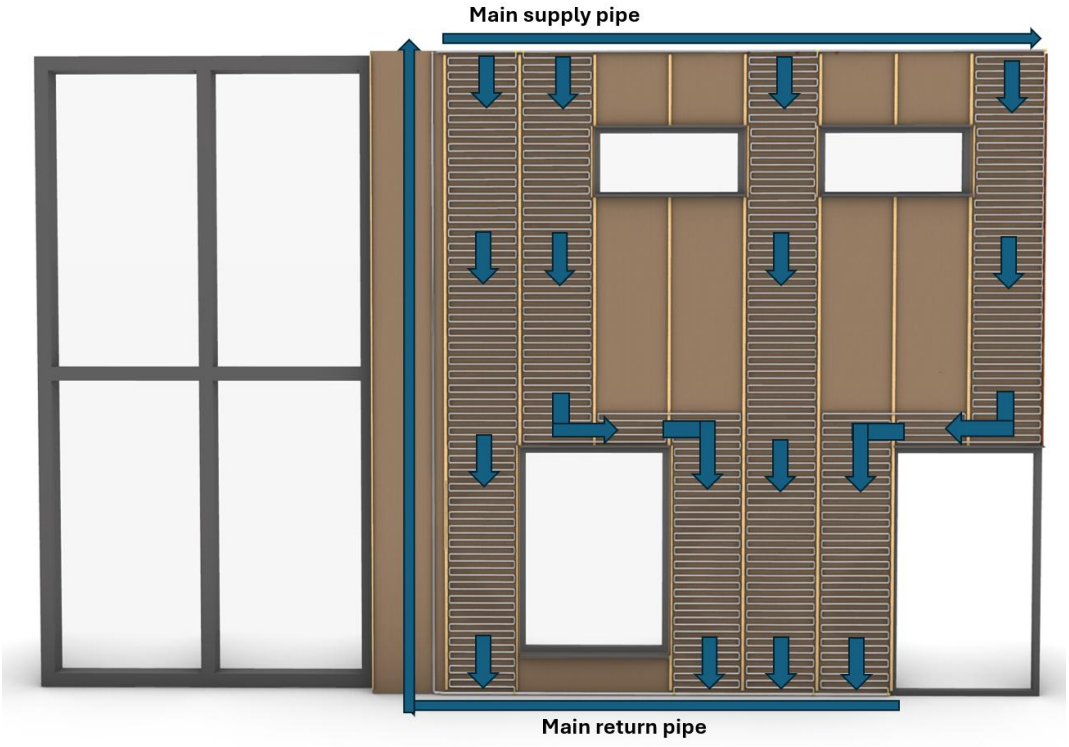

Figure 42 Serpentine pipe layout of A-Brick ASTF when applying on a building. B*y author*

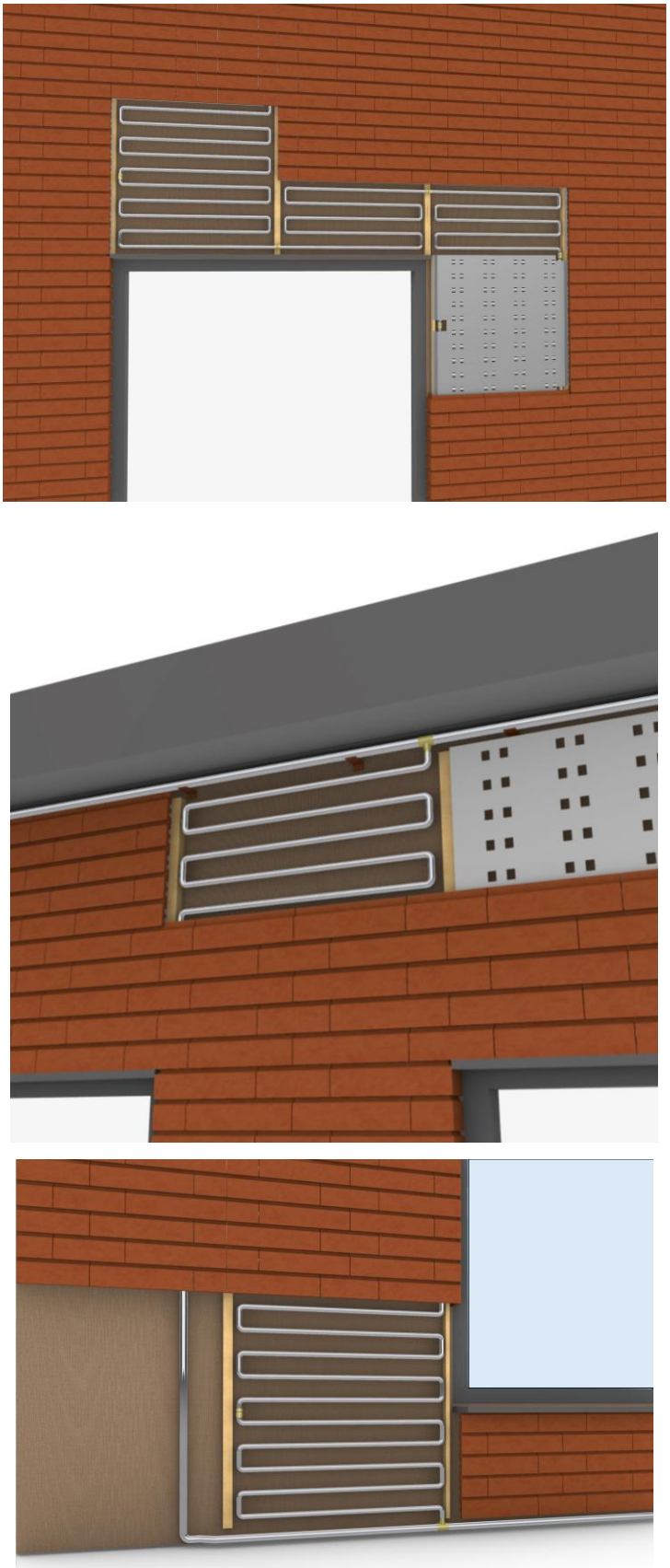

Figure 43: Details at top, bottom and window. B*y author*

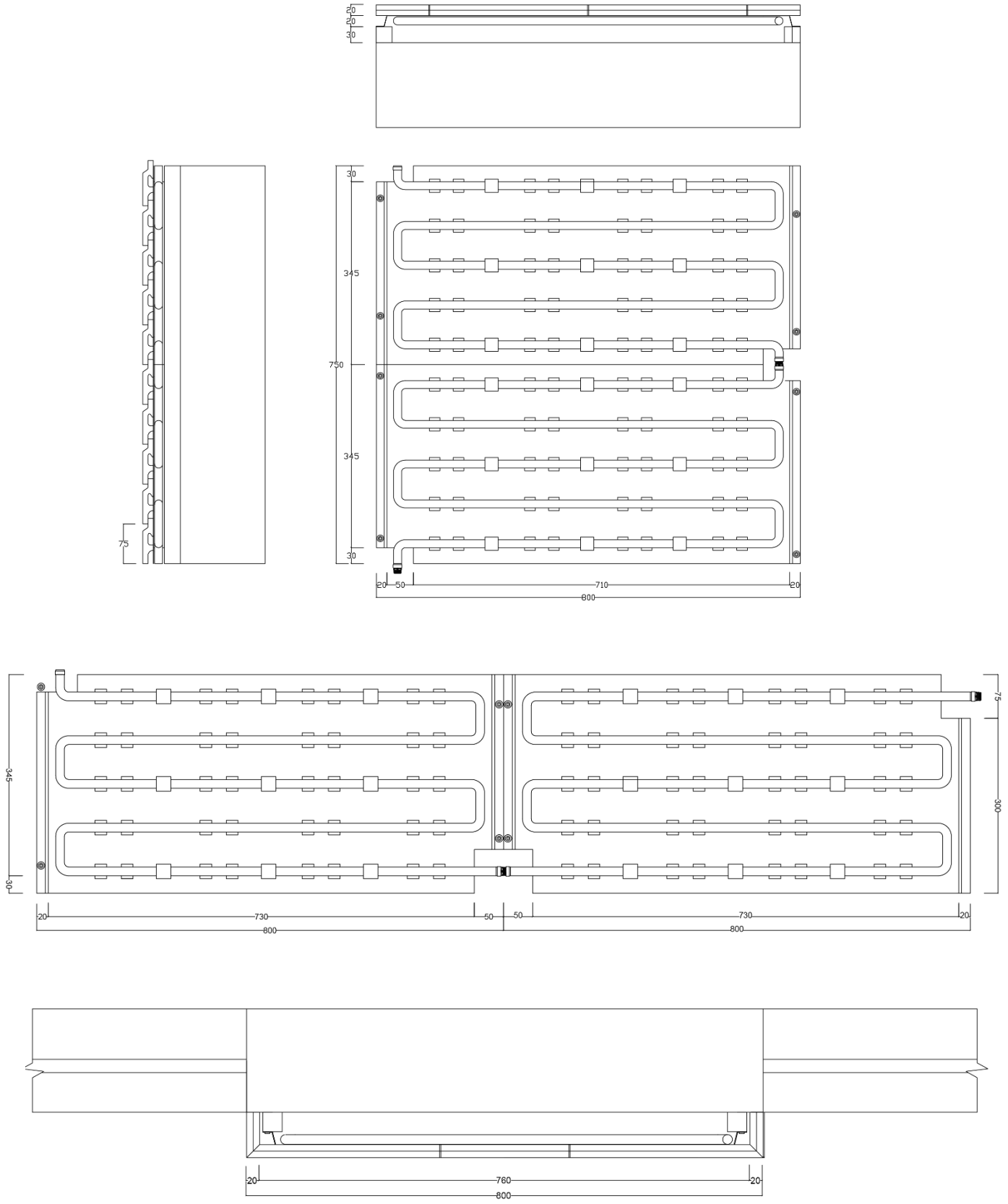

Figure 44: Technical drawings of vertical unit, horizontal unit and window unit. B*y author*